Materials Today Bio 31 (2025) 101522

Contents lists available at ScienceDirect

Materials Today Bio

journal homepage: www.journals.elsevier.com/materials-today-bio

Engineering dual-driven pro-angiogenic nanozyme based on porous silicon for synergistic acceleration of burn infected wound healing

Wei Duan [a,b,d,e], Yue Gao [a], Ruru Xu [a], Sheng Huang [a], Xueqian Xia [a], Jingwen Zhao [b], Longhuan Zeng [c], Qiaolin Wei [a,d,e], Jia-Wei Shen [a,d,**], Jianmin Wu [b,***], Yongke Zheng [c,*]

[a] School of Pharmacy, Hangzhou Normal University, Hangzhou, 311121, PR China
[b] Lab of Nanomedicine and Omic-based Diagnostics, Institute of Analytical Chemistry, Department of Chemistry, Zhejiang University, Hangzhou, 310058, PR China
[c] Department of Rehabilitation, Affiliated Hangzhou First People's Hospital, School of Medicine, Westlake University, Hangzhou, 310006, PR China
[d] Key Laboratory of Elemene Class Anti-Cancer Chinese Medicines, Engineering Laboratory of Development and Application of Traditional Chinese Medicines, Collaborative Innovation Center of Traditional Chinese Medicines of Zhejiang Province, Hangzhou Normal University, Hangzhou, 311121, PR China
[e] State Key Laboratory of Silicon and Advanced Semiconductor Materials, Zhejiang University, Hangzhou, 310027, PR China

ARTICLE INFO

Keywords:
Burn infected wounds
Nanozyme
Porous silicon
Angiogenesis
Photothermal therapy

ABSTRACT

The high mortality risk of burn infected wounds has dictated the clinical need for the development of new biomaterials that can regulate multiple aspects of the healing process in a high-quality manner. Although nanozymes have made progress in inflammation modulation and antibacterial management, they often lack the ability in pro-angiogenesis, which greatly limits their functional application in the synergistic treatment of burn infected wounds. In this study, a smart pro-angiogenic nanozyme is simply and efficiently synthesized by *in situ* reduction of Pt precursors on porous silicon (PSi) nanocarriers. Owing to the hybridization of Pt, the Pt-decorated PSi (Pt@PSi) nanocomposites exhibit excellent near-infrared (NIR) photothermal activity and peroxidase-like catalytic activity, which can be used for co-efficient antibacterial treatment. After exposure to 808 nm NIR laser, Pt@PSi-based photothermal and nano-catalytic combined therapy can achieve more than 95 % bacterial inhibition *in vitro*. More importantly, under the stimulation of NIR laser and nanozyme, the smart Pt@PSi nanocomposites can efficiently release bioactive inorganic Si ions from the PSi skeleton, which can efficiently promote endothelial cell migration, tube formation, and angiogenesis. Furthermore, *In vivo* animal studies have demonstrated that Pt@PSi-based combination therapy can significantly accelerate the healing of infected burn infections by inhibiting bacterial growth, scavenging reactive oxygen species, and promoting angiogenesis with a favorable biosafety. Overall, the dual-driven pro-angiogenic nanozyme based on PSi expands the functional application of nanozyme, providing a novel combined strategy for efficient care of difficult-to-heal burn infected wounds.

1. Introduction

Burns, usually caused by heat, flame, electricity, and chemicals, are one of the most devastating traumas [1,2]. Clinically, burn wounds healing are usually hampered by impaired regeneration of deep dermal tissues and persistent infections, which may even lead to sepsis [3]. Burn infected wounds pose a serious threat to the patient's life and health. According to the World Health Organization (WHO), more than 11 million people worldwide suffer from burn injuries each year with a high mortality rate, estimated at more than 250,000 deaths per year [4]. Compared to normal wounds, the microenvironment of burn wounds has a series of complex features such as over-expression of reactive oxygen species (ROS), long-term of inflammation, increased risk of bacterial infection, and insufficient levels of vascularization, which will further limit the healing process [5,6]. Although traditional pharmacological treatments such as antibiotics are capable of treating burn

* Corresponding author.
** Corresponding author. School of Pharmacy, Hangzhou Normal University, Hangzhou, 311121, PR China.
*** Corresponding author.
E-mail addresses: shen.jiawei@hotmail.com (J.-W. Shen), wjm-st1@zju.edu.cn (J. Wu), zhengyongke@hospital.westlake.edu.cn (Y. Zheng).

https://doi.org/10.1016/j.mtbio.2025.101522
Received 24 November 2024; Received in revised form 9 January 2025; Accepted 24 January 2025
Available online 24 January 2025

infected wounds to a certain extent, the single therapeutic function of antibiotics is unable to satisfy the clinical need for multiple management for burn infected wounds in terms of scavenging ROS, regulating inflammation, promoting vascularization to accelerate the rate of wound healing [7,8]. In addition, overuse of antibiotics can lead to increased bacterial resistance, thus compromising therapeutic efficacy [9]. Therefore, there is an urgent need to design and develop highly effective and safe therapeutic systems with multiple therapeutic functions to accelerate the healing process of hard-to-heal burn infected wounds.

In recent years, continued breakthroughs and advances of nanomaterials in biomedical field have provided opportunities for the development of highly effective antibiotic-free therapies capable of effectively preventing infections and promoting healing of burn infected wounds [10,11]. To date, nanomaterials have been shown to inherently exhibit multiple functions in wound therapy such as targeted delivery, bioactive ion release, photothermal properties, and photodynamic effects, which can enhance interactions with bacteria and improve the combined antimicrobial effect [12–14]. For example, several nanomaterials such as metal oxides, noble metals, carbon nanomaterials, metal-organic framework (MOF), have been used as photothermal agents to induce localized high temperature under the irradiation of near-infrared (NIR) light to achieve non-invasive photothermal therapy (PTT) through bacterial protein denaturation and irreversible bacterial destruction [15–17]. On the other hand, many nanomaterials have also been shown to have bionic-like enzyme activity, and these materials are also called as nanozymes [18,19]. Nanozymes can address many of the challenges associated with natural enzymes such as potential antigenicity, poor bioavailability, and low stability under pathological conditions, showing great potential as alternatives to natural enzymes in wound therapy applications [20,21]. Currently, nanozymes are effective in regulating ROS levels and inflammatory microenvironment with efficient bactericidal ability [22,23]. Moreover, nanozymes can be further combined with other therapies (e.g., photothermal, photodynamic, magnetothermal, etc.) to activate and amplify the specific therapeutic effect, which is now becoming a research hotspot in the field of wound treatment. For example, Zhao et al. separately synthesized MXene and Fe-MOF nanomaterials, and prepared hybrids of the two materials through physical interactions [24]. They found that the novel composite material possesses peroxidase (POD)-like catalytic activity and both photothermal and photocatalytic properties could be improved under NIR light irradiation. Their study demonstrated that the combination of PTT with nanocatalytic therapy can be utilized as a novel strategy for stimuli-responsive antimicrobial therapy. Although nanozymes have been widely used in modulating ROS and antimicrobials for wound treatment, their synthesis steps are complex and their activity is low or unstable in physiological environments [25–27]. Besides, poor vascularization of burn wounds can severely limit oxygen and nutrient delivery to the wound site, complicating the healing process and prolonging healing time [28,29]. There are very few nanozymes currently exhibiting pro-angiogenic capacity [30–32], greatly limiting the functional application of nanozymes in the synergistic management of burn infected wounds.

Silicon-based biomaterials are considered one of the most promising biomaterials in the field of nanomedicine due to their abundant raw material source, tunable micro/nano structure, diverse surface functionalization, multiple bioactivity and good biocompatibility [33]. Porous silicon (PSi) materials, prepared by electrochemical etching of monocrystalline silicon wafers at room temperature, have been widely studied for efficient wound care due to their simple preparation process, high specific surface area, tunable pore structure, easy surface modification, and good biocompatibility and degradability [34–36]. Our previous work demonstrates that non-toxic silicon ions, the only degradation product of PSi in living organisms, can stabilize the expression of vascular growth factor (VEGF) and hypoxia-inducible factor (HIF-1a), promoting the migration and vascularization of skin cells [37]. Hence, PSi-based nanomaterial has great potential for angiogenesis therapy of various disease, including chronic wounds. However, PSi has limited antimicrobial efficiency, which restrict their effectiveness for burn infected wounds treatment. To address this challenge, utilizing the rich pore structure of PSi to load nanozymes with efficient antimicrobial activity is expected to be a promising strategy. Moreover, the porous structure of PSi can effectively prevent the interference of biological matrices in body fluids on the enzyme activity and improve the catalytic activity and stability through nanoconfinement effect, making PSi an effective carrier for nanozymes [38,39]. Therefore, it is imperative to rationally design and construct functionalized PSi-based nanozyme with multiple stimulus responses for combined antibacterial, anti-inflammatory, and pro-angiogenic treatments of burn infected wounds in a more precise and efficient way.

Based on the above considerations, here, we fabricate a novel Pt-decorated PSi (Pt@PSi) composites driven by NIR light and nanozyme for synergistically accelerating burn infected wound healing (Scheme 1). During the preparation process, PSi nanoparticles (NPs) are firstly obtained by several steps including electrochemical etching of Si wafer, lift-off of PSi layer and ultrasound of PSi film. Afterwards, PSi NPs are used as template for *in situ* reduction of the noble metallic precursor, and Pt metallic NPs are generated and confined on PSi support. The synthesized Pt@PSi material has the following advantages compared to other Pt materials. First, compared to other methods of synthesizing Pt NPs, using PSi as a template and reducing agent has the advantages of simplicity, efficiency, and aqueous phase processing, without the need for high temperature, high pressure and organic solvent. Second, Pt@PSi can effectively prevent the aggregation of Pt NPs with high surface energy, and reduce the usage of Pt to improve the benefit-to-risk ratio. Finally, the bioactivity of the PSi, which mainly includes the regulation of cell behavior and promotion of vascularization, can effectively endow the nanozyme with richer functional characteristics for the integrated care of infected burn wounds. Benefited from the Pt doping, the smart Pt@PSi nanocomposites show improved NIR photothermal conversion activity and high POD-like catalytic activity. Further, the release of Si ions from the nanocomposites can also be driven by both endogenous ROS stimuli and exogenous NIR light stimuli. This NIR light and ROS dual-driven system can trigger the combined photothermal/nanocatalytic/ion therapy for the highly effective antibacteria and pro-angiogenesis both *in vitro* and *in vivo*, which has great potential in the clinically drug-free treatment of burn infected wounds and even other refractory infected wounds.

2. Experimental section

2.1. Preparation of PSi NPs

PSi NPs were synthesized using a previous top-down approach *via* a Teflon etch cell and a platinum counter-electrode. The etching of PSi nanostructure was carried out on the commercial electrochemical integrated device (Well-healthcare Technologies Co.). In brief, a layer of PSi was firstly formed on boron-doped silicon wafer (resistivity: 0.0005−0.0012 Ω/cm) by electrochemical etching (constant current mode, current density: 77 mA/cm^2) in an electrolyte (hydrofluoric acid: ethanol = 4:1) at room temperature. Then, the PSi layer was separated from the silicon wafer by an electrochemical-assisted method (constant current mode, current density 22 mA/cm^2) in an electrolyte with lower hydrofluoric acid concentration (hydrofluoric acid: ethanol = 1:12) to obtain free PSi films. Finally, the stripped PSi films were sonicated (500 W, 3 h) in ethanol, the supernatant was washed with ethanol three times by centrifugation at 10000 rpm for 10 min to remove the ultrasmall particles, the bottom product was collected and nano-sized PSi particles were obtained.

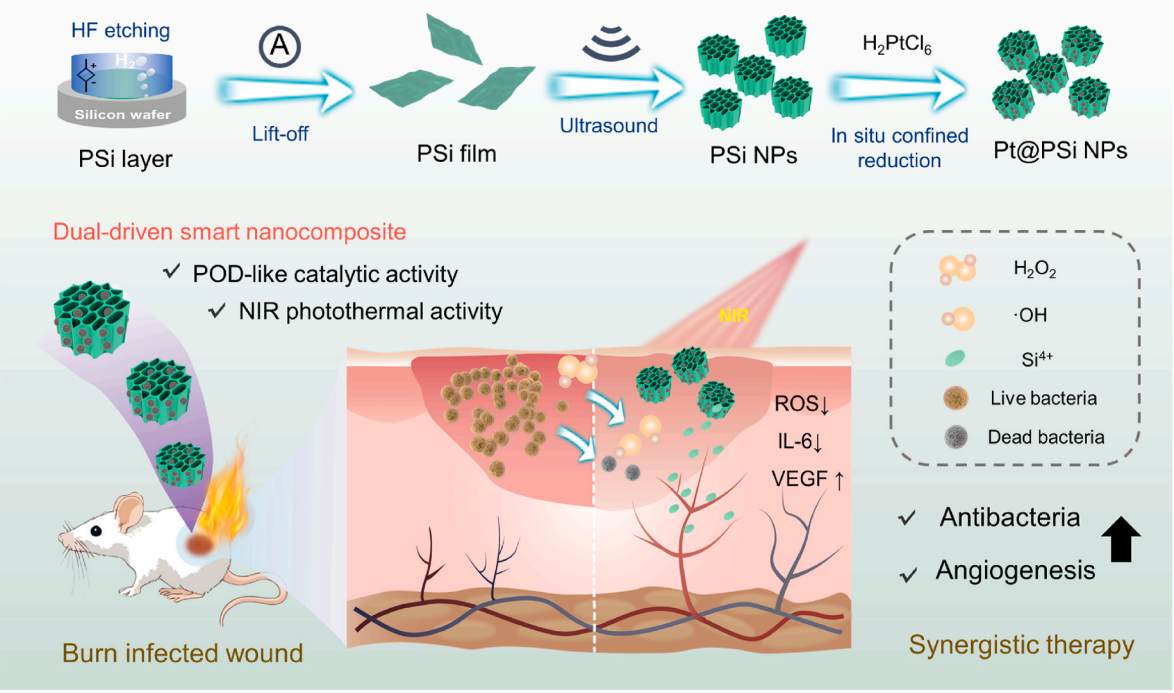

Scheme 1. Schematic representation for the preparation process of dual-driven smart Pt@PSi nanocomposites with nanozyme and photothermal activity for synergistic therapy of burn infected wound.

2.2. Preparation of Pt@PSi nanocomposites

To prepare Pt@PSi nanocomposites, 1 g of the prepared PSi NPs was added to 2 mL of aqueous solution. Next, 100 μL of 20 mg/mL citric acid solution was added and stirred thoroughly. Then, the above mixed solution was heated to 60 °C in a water bath. Next, 20 μL H_2PtCl_6 (50 mM) was quickly added to the above mixture and the reaction was continued for 2 h. Afterwards, the dark black Pt@PSi nanocomposites was collected and washed 3 times by deionized water to remove excess reactants. Finally, the bottom Pt@PSi product was collected and stored at 4 °C for further use.

2.3. Characterization

The transmission electron microscopy (TEM) micrographs were taken by a JEM 1400 microscopy (JEOL). High-angle annular dark-field scanning transmission electron microscopy (HAADF-STEM) was performed using a JEM-2100F microscope (JEOL). X-ray elemental mapping (EDX) measurements were carried out on a Tecnai F30 microscope (Philips). The X-ray photoelectron spectroscopy (XPS) data was carried out using a ESCALAB 250XI instrument (Thermo Fisher). The zeta potential and size contribution were analyzed by a Nano-ZS90 m (Zetasizer). The powder X-ray diffraction (XRD) was collected *via* X-ray diffractometer (Shimadzu) with Cu Kα radiation (λ = 1.542 Å). The fourier transform infrared (FTIR) spectra was tested on a SCIENTIFIC NICOLET iS10 spectroscopy (Thermo Fisher). The UV–vis absorption spectra were recorded with a UV-2450 spectrometer (Shimadzu).

2.4. Photothermal properties

The photothermal properties were tested in a 48-well plate and irradiated by a vertical NIR laser with a spot diameter of 1 cm at a distance of 10 cm. To compare the photothermal conversion ability of different materials, an aqueous solution containing 500 μL of PSi and Pt@PSi materials (200 μg/mL) was irradiated with 808 nm NIR laser. Thermal images were acquired by commercial FLIR ONE thermal imager (FLIR System) at specific intervals of time, and temperature changes were recorded. Subsequently, the dependence properties of the photothermal performance of the Pt@PSi materials were evaluated by varying the test conditions such as concentration and laser power. In addition, the photothermal stability of Pt@PSi was tested by three laser switching cycle experiments. The photothermal convention efficiency (η) of Pt@PSi was calculated based on the typical method according to our previous work [40].

2.5. Nanozyme catalytic effects

The steps for investigation of nanozyme catalytic effects are as follows: 100 μL of PSi or Pt@PSi NPs (2 mg/mL) were added into 900 μL of phosphate buffer solution (PBS) solution (50 mM, pH = 6.5) containing H_2O_2 (10 mM) and 3,3′,5,5′-tetramethylbenzidine (TMB) (0.5 mM). Then, the absorbance was measured by a UV spectrophotometer after reacting for 10 min at room temperature. At the same time, changes of absorbance value at 652 nm in 10 min was recorded. To validate the catalytic mechanism, the production of free radicals in different catalytic reactions was determined by electron spin resonance (ESR, Bruker EMX) spectrometer. DMPO is used as a capture agent and the mixed solution was measured in a quartz capillary. To evaluate the ROS scavenging capability of materials *in vitro*, commercial assay kits were employed to measure the levels of H_2O_2 and $\bullet O_2^-$ after treatment with different groups and the scavenging efficiency was calculated according to established procedures and methods [41,42].

To explore the steady-state kinetics of catalytic reactions, the POD-like activity of Pt@PSi nanozyme in the absence or in the presence of NIR laser (1 W/cm^2, 10 min) for different concentrations of H_2O_2 was tested according to the absorbance value at 652 nm of the chromogenic system. The associated enzyme dynamic parameters (K_m and V_{max}) were calculated according to the following Michaelis-menten equation: $1/V_0 = (K_m/V_{max})(1/[S] + 1/V_{max})$, V_0, V_{max}, [S] and K_m represent initial velocity, maximum reaction velocity, substrate concentration and Michaelis constant, respectively.

In order to study the effects of temperature on the relative activity, the absorption value at 652 nm of Pt@PSi nanozyme-triggered H_2O_2-TMB system at different temperatures was monitored after the reaction

was complete (10 min). The relative activity of different groups was calculated with the maximum absorption value of 100 %.

In order to study the effects of storage time on the relative activity, Pt@PSi nanozyme stored for different times at room temperature was added to the above reaction system, and the absorption value at 652 nm was monitored after the reaction was complete (10 min). The relative activity of different groups was calculated with the maximum absorption value of 100 %.

2.6. Si ions release study

To test ion release behavior, 500 μg/mL Pt@PSi nanocomposites were incubated in PBS (pH = 6.5) at 37 °C and the supernatant was collected at different time points. Besides, Si ions release in PBS containing a high ROS level (1 mM H_2O_2) and NIR laser treatment (1 W/cm^2, 10 min per day) was also studied. The release content of inorganic silicon ions in the supernatant was measured by inductively coupled plasma emission spectrometer (ICP-OES, Varian 715-ES) and the cumulative release percentage was calculated. Each test group contained three parallel samples.

2.7. In vitro antibacterial and antibiofilm test

The antibacterial activity was evaluated by *Staphylococcus aureus* (*S. aureus*) as bacterial model. First, the bacteria were grown overnight in liquid medium on a constant temperature shaker (37 °C). Subsequently, PSi and Pt@PSi NPs were added to a 5×10^6 CFU/mL bacterial suspension at a final concentration of 500 μg/mL. To mimic the wound environment, the solution also contained 1 mM of H_2O_2. In particular, the Pt@PSi + NIR group was irradiated with a NIR laser (1.0 W/cm^2) for 10 min. Then, 10 μL of the treated medium was collected and the OD_{570} value of each group of bacteria was determined by microplate reader (Tecan, Infinite M200 Pro) after cultured in 96-well plate for different time. At the same time, 10 μl of bacterial suspension was smeared on the plate containing nutrient agar after dilution of 10^4 times. After incubation at 37 °C for 12 h, the colonies were photographed and quantitative analysis with ImageJ software. In order to observe the morphology of the bacteria after treatment, the bacterial cells were fixed with 2.5 % glutaraldehyde for 12 h and then suspended in ethanol solution. The bacterial cells were subjected to gradient dehydration in different ethanol concentrations. Finally, the morphology of bacteria was characterized by SU8020 field emission scanning electron microscopy (SEM, Hitachi). To further demonstrate the efficacy of bacterial treatment, bacterial cells were stained with SYTO/PI dye (MKbio) for 15 min, washed three times with PBS, and then observed for live (green fluorescence) and dead (red fluorescence) bacteria with fluorescence microscope (Olympus, IX73). To further demonstrate the antibiofilm effect, high concentration of *S. aureus* (10^8 CFU/mL) was incubated in 24-well plates. After 48 h of incubation at 37 °C, the culture medium was gently aspirated and then treated with different groups. Subsequently, remaining *S. aureus* biofilm was quantified by the classical crystal violet (0.1 %) staining method. The absorbance at 570 nm was recorded using the microplate reader and remaining biofilm percent was calculated according to our previous work [43]. Finally, the biofilms were stained with SYTO/PI dye (MKbio) and observed using a fluorescence confocal microscope (Nikon Eclipse Ti A1, Japan).

2.8. In vitro blood compatibility test

The blood compatibility of Pt@PSi nanocomposites was determined by hemolysis. Specifically, 1 mL fresh blood was taken and washed with 10 mL PBS (0.01 M) for 3 times, and 2 % red blood cells (RBCs) suspension was obtained by PBS re-suspension. After that, different concentrations of Pt@PSi (100, 200, 500 μg/mL) were dissolved in 0.8 mL PBS and mixed with 0.2 mL RBCs solution. In the NIR on group, Pt-PSi nanocomposites was irradiated with 808 nm NIR light (1 W/cm^2, 10 min). PBS and deionized water were the negative control group and positive control group, respectively. After incubating at 37 °C for 12 h, the mixture was centrifuged (3000 rpm, 6 min). The absorption of supernatant by measuring the OD value at 570 nm using the microplate reader. The percent of hemolysis was calculated as follows: Hemolysis (%) = $[(OD_{sample} - OD_{control})/(OD_{positive\ control} - OD_{negative\ control})] *100$.

2.9. In vitro cell compatibility test

Human umbilical vein endothelial cells (HUVECs, Sciencell) were cultured in a humidified 37 °C/5 % CO_2 incubator for further use. To evaluate the cell compatibility, HUVECs were cultured in 96-well plates for 24 h and Pt@PSi nanocomposites were then added to the culture medium at different concentrations. The NIR on group was irradiated with 808 nm laser for 10 min (1.0 W/cm^2). After that, the cells were cultured for another 48 h, and the medium was replaced by 150 μL of CellTiter-Lumi (Beyotime) reagent was added, and the luminescence intensity of the cells after co-incubation with the material was measured with a multifunctional microplate reader (Tecan, Infinite M200 Pro). The viability of cells was calculated as follows. Cell viability (%) = $[(OD_{sample} - OD_{background})/(OD_{control} - OD_{background})] *100$, where OD_{sample} is the optical density of the experimental sample, $Od_{background}$ is the optical density of blank, and $OD_{control}$ is the optical density of the control sample.

2.10. In vitro scratch assay

To test the cell migration behavior, HUVECs (5×10^4 per cell) were firstly seeded and grown overnight to form a monolayer onto a 6-well plate. Then, a pipette tip was used to create a straight scratch across the HUVECs monolayer. Subsequently, cells were washed with PBS (0.01 M) for 3 times. After that, fresh cell culture medium containing Pt@PSi (200 μg/mL) was added. For NIR on group, cells were irradiated with 808 nm laser (1.0 W/cm^2) for 10 min. Finally, the scratch was observed using optical microscope after coincubation for another 4 h an 12 h. The scratch area was measured by Image J software.

2.11. In vitro ROS scavenging assay

To further validate ROS scavenging, the HUVECs (10^4 per cell) were firstly seeded and grown overnight to form a monolayer onto a 48-well plate. After that, fresh culture medium containing Fenton's reagent (400 μM of H_2O_2 and 40 μM of $FeSO_4$) was incubated with these cells for another 2 h. Following this, the HUVECs were washed with PBS three times. Subsequently, fresh cell culture medium containing PSi and Pt@PSi (200 μg/mL) was added. The Pt@PSi + NIR group was irradiated with 808 nm laser (1 W/cm^2) for 10 min. After 0.5 h of incubation, the ROS-sensitive fluorescent dye 2′,7′-dichlorofluorescein diacetate (DCFH-DA) was used for cell staining and imaging according to the manufacturer's instructions. Finally, the images were captured with fluorescence microscope (Olympus, IX73).

2.12. In vitro tube formation assay

The *in vitro* tube formation experiments of HUVECS were performed according to previous steps [37]. First, HUVECs were seeded at a density of 10^4 per well in a 24-well culture plate, which is uniformly precoated with Matrigel in advance. Subsequently, 10 μL of PBS containing PSi and Pt@PSi was added to the medium. The Pt@PSi + NIR group was irradiated with 808 nm laser (1 W/cm^2) for 10 min. After 6 h of incubation, cells were stained with Calcein AM dye and observed by fluorescence microscope (Olympus, IX73). The number of tubes formed was calculated with ImageJ software.

2.13. In vivo CAM assay

Based on previous studies, *in vivo* angiogenesis of the composite was tested by chorioallantoic membrane (CAM) experiments [37]. First, fertilized eggs were incubated in a 38 °C incubator at a suitable humidity for 7 days. Then, a syringe was used to carefully inject the PBS solution containing PSi, Pt@PSi (200 μg/mL) on the CAM of the 7-day-old chicken embryo. The Pt@PSi + NIR group was irradiated with 808 nm laser (1 W/cm^2) for 10 min. The seeded eggs were then continued to be incubated at 38 °C for 1 day and the top window was opened at Day 8 and imaged using a digital camera (Canon). Several angiogenesis parameters such as total length, size, and ligation after treatment with different nanomaterials were quantified using AngioQuant software (version 1.33, Mathwork Inc.).

2.14. In vivo wound-healing experiments

In this study, all animal-related operations and procedures were conducted in accordance with the Hangzhou Normal University institutional animal care and use committee guidelines. Twenty BALB/c mice (6 weeks) were randomly divided into Control (PBS), PSi, Pt@PSi, and Pt@PSi + NIR groups. A burn wound model was established by electrically heating a flat-headed metal rod to 100 °C and contacting the skin of the back of the rats for 30 s. Afterwards, the wound was pruned with surgical scissors. The suspension containing 10^7 CFU/mL *S. aureus* was then added to infect the wound for one day and the hard-to-healing burn infected wound model was established. During the healing process, PBS solution containing different materials was sprayed on the wound surface every two days. The laser group was treated with NIR light (1 W/cm^2, 10 min) every two days. The wound healing process was observed in two weeks, and the wound images was recorded by iPhone 13 (Apple) and the wound healing rate was analyzed by ImageJ software. After treatment, the mice in each group were killed, and the bacteria in the wound tissue were counted and analyzed. H&E, Masson's trichrome staining, ROS staining and immunofluorescence staining (IL-6, VEGF) were conducted and the collagen maturation, inflammation, re-epithelization and the expression of related proteins were analyzed. At the same time, the changes of body weight, histochemical staining of main organs and blood test were conducted to evaluate the biosafety of the new therapy.

2.15. Statistical analysis

All experiments were carried out at least in triplicate. The experimental data was analyzed by one-way analysis of variance (ANOVA) function in Microsoft Excel 2021. Results are presented as mean ± standard deviation.

3. Results and discussion

3.1. Synthesis and characterization

In this study, PSi NPs were prepared by a top-down electrochemical etching method based on our previous work [40,43,44]. As shown in Scheme 1, a PSi layer is formed on the surface of silicon wafer after constant current electrochemical etching with HF as electrolyte. Next, PSi NPs are obtained by lift-off and ultrasound of the obtained PSi layer. One advantage of the top-down approach is that the size of PSi particles can be easily controlled depending on ultrasound time and power. The prepared PSi particles were firstly characterized by TEM. As shown in Fig. S1, the as-prepared PSi NPs with particle size of ~200 nm show abundant vertical channels, which can support the confinement and loading of drugs and small size metallic NPs.

Subsequently, Pt NPs were confined and grown in the PSi framework using *in situ* self-reduction method. Our previous work has shown that PSi material has a high reduction capacity due to the presence of abundant Si-H$_x$ bonds, and can serve as both templates and reducing agents for deposition of small-size metallic NPs such as Ag, Pd and Cu [38,43,45]. During the reaction process, the Pt precursor gets electrons from the surface hydride of PSi (Si-Hx) and is reduced to metallic Pt substance. The addition of citric acid during the reaction can increase the acidity of the precursor solution and inhibit the hydrolysis of noble metal salts. At the same time, the carboxyl functional groups on the surface of citric acid can effectively adsorb metal cations, thus ensuring uniform nucleation of metal salts on the surface of PSi template during the *in situ* reduction [46]. Fig. 1a shows a representative TEM image of the prepared Pt@PSi nanocomposites. As shown, the dark black Pt spherical NPs with small size on the PSi substrate can be clearly observed, and the distribution of Pt NPs is dense and uniform. In addition, HAADF-STEM image in Fig. 1b shows isolated and distinguishable bright spots from the composite, which is attributed to Pt NPs. Furthermore, the uniform distribution of Pt, Si, and O elements in the composite can be found by STEM elemental mapping results, indicating the successful synthesis of Pt@PSi materials (Fig. 1c). As shown in Fig. 1d, the average particle size of the composite is found to be 267.8 nm with a polydispersity index (PDI) value of 0.227 by DLS testing, which is basically in agreement with that observed in TEM image. As demonstrated in Fig. S2, Pt@PSi has a potential of −24.4 mV, indicating that it is relatively stable in aqueous solution.

In order to further investigate the reaction mechanism, PSi and Pt@PSi samples were characterized by XRD and FTIR technique. As shown in Fig. 1e, two obvious XRD diffraction peaks of synthesized PSi NPs located at 2θ values of 28.7°and 76.7° can be assigned to the Si crystal of (111) and (100), respectively [47]. However, Pt@PSi nanocomposites show a broad band of amorphous silicon dioxide and diffraction peaks of Pt. Three diffraction peaks of Pt (111), (200), and (220) indicate that the H_2PtCl_6 precursor is successfully reduced to Pt with face-centered cubic (FCC) phase [48]. The XRD results show that PSi is oxidized and the structure is greatly changed during the reaction. In addition, the FTIR results indicate there are two obvious absorption peaks at ~916 cm^{-1} and ~2100 cm^{-1}, which belongs to the scissoring and telescopic vibration of abundant Si-H$_x$ on the PSi surface [49] (Fig. 1f). After Pt hybridization, the absorption peak of Si-H$_x$ in Pt@PSi disappears obviously, indicating that it is consumed in the self-reduction reaction. At the same time, the infrared absorption peak of Pt@PSi nanocomposite at ~1100 cm^{-1} is attributed to the tensile vibration of Si-O-Si, which further confirms the oxidation of PSi as a template and reducing agent [43]. This phenomenon is attributed to the redox reaction between the noble metal precursor and the strongly reducing Si-H$_x$ in the self-reduction reaction. In this reaction, H_2PtCl_6 is reduced to Pt metal, while Si-H$_x$ is oxidized to Si-O-Si.

Moreover, XPS was used to analyze the composition and valence states of the elements in the nanocomposites. As revealed in Fig. 1g, the presence of Pt, Si, and O components in Pt@PSi can be clearly observed from the XPS full spectrum. Besides, the high-resolution XPS spectrum of Si 2p consists of two main peaks (2p 1/2 and 2p 3/2), where one of the main peaks with binding energy at 103.76 eV represents silicon oxide and the other with binding energy at 99.11 eV refers to Si, respectively (Fig. 1h) [43]. In the high resolution XPS spectra of Pt, two peaks appeared at 74.2 eV and 71.9 eV are attributed to 4f 5/2 and 4f 7/2, respectively, proving that Pt is a zero-valent singlet state in the nanocomposite [48]. (Fig. 1i). These above results demonstrate the successful preparation of Pt@PSi composite materials.

3.2. Photothermal, nanozyme and Si release performance

It has been widely reported that various types of Pt-based nanomaterials have excellent NIR absorption and photothermal conversion capabilities [50–52]. Therefore, Pt@PSi is expected to break the limitation of PTT application for PSi materials. Inspired by the existing work, we first investigated the absorption property of the prepared Pt@PSi by UV–vis spectroscopy. As shown in Fig. 2a, thanks to the Pt doping,

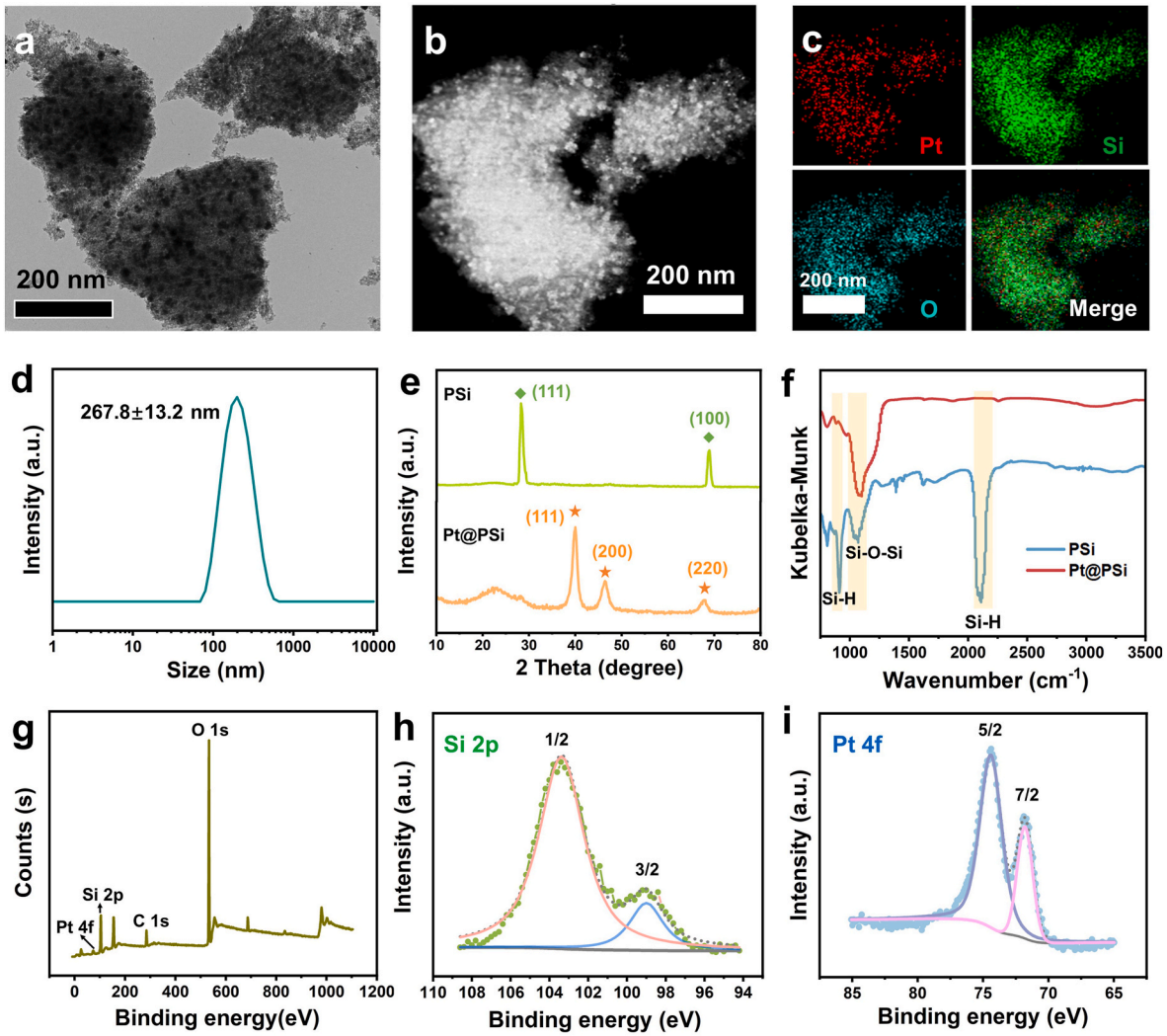

Fig. 1. Characterization of Pt@PSi nanocomposites prepared by *in situ* confined reduction method. (a) Representative TEM image of as-prepared Pt@PSi nanocomposites. (b) HAADF-STEM image of Pt@PSi nanocomposite. (c) Element mapping result including Pt, Si, O and merge images of Pt@PSi nanocomposite. (d) Hydrodynamic diameter of Pt@PSi nanocomposite measured by DLS. (e) XRD pattern of PSi NPs and Pt@PSi nanocomposite. (f) FTIR spectra of PSi NPs and Pt@PSi nanocomposite. (g) The XPS full spectra of Pt@PSi nanocomposite. The high-resolution XPS spectra of Si 2p (h) and Pt 4f (i) for Pt@PSi nanocomposite.

Pt@PSi has a stronger absorption in the NIR region compared to PSi alone, which is favorable for enhancing photothermal conversion ability. The 808 nm laser is located in the NIR spectral region (700–1100 nm), which is known as the "optical window" for biological tissues [16,52]. Light in this wavelength range experiences less scattering and absorption, allowing it to penetrate deeper into tissues [24]. Compared to red light at 600 nm, the 808 nm light has a greater penetration depth in biological tissues, enabling it to reach deeper layers more effectively. Compared to another commonly used 1064 nm laser, although it has even greater penetration depth, the depth achieved by the 808 nm laser is sufficient for treating superficial tissues such as wounds [31]. Additionally, 808 nm laser with relatively common equipment and lower cost is widely used in the medical field, making them convenient for practical applications. Here, we tested the heating temperature of the solution of Pt@PSi under the irradiation of a vertical NIR laser (808 nm, 1 W/cm^2) using a thermal imager. As shown in Fig. 2b and c, rapid temperature rise of the aqueous solution containing Pt@PSi material is observed under NIR laser irradiation. After irradiation for 10 min, the plateau can be reached at 50.3 °C for the Pt@PSi group, which is ~20 °C higher than PSi. Further, the heating curves of different concentrations of Pt@PSi under the NIR light indicate that the photothermal activity of the material is concentration-dependent (Fig. 2d). Additionally, Fig. 2e shows that the photothermal ability of the Pt@PSi nanocomposite is closely related to the laser power density. The five cycle tests in Fig. 2f show that the photothermal properties of the Pt@PSi material are stable and can be used for several times with almost no change. Moreover, the photothermal conversion efficiency (η) of the Pt@PSi was calculated as 33.4 % (Fig. S3). The above experimental results demonstrate the excellent NIR photothermal conversion capability of the Pt@PSi nanocomposites.

Another property of smart Pt@PSi nanocomposites lies in the nanozyme activity derived from Pt NPs. Notably, our previous work showed that the pore channel of PSi present nano-confinement effect that will significantly enhance the catalytic activity and stability of POD nanozymes [38]. Here, in order to examine the POD catalytic performance of the composites, the classical color development reaction of H_2O_2 and TMB is used. The main reaction principle involves the catalytic decomposition of the H_2O_2 substrate by the POD-like nanozymes to generate hydroxyl radicals (·OH), which can effectively catalyze the oxidation and discoloration of TMB. The oxidized TMB has a maximum absorption peak at 652 nm, which can be exploited as indicator to study the catalytic activity of Pt@PSi nanozyme. As known, due to the presence of bacterial metabolites, wound infection sites are typically acidic microenvironments with a pH range of 5.0–6.5 [53,54]. Here, the catalytic activity of nanozyme is tested in PBS at a pH value of 6.5. As

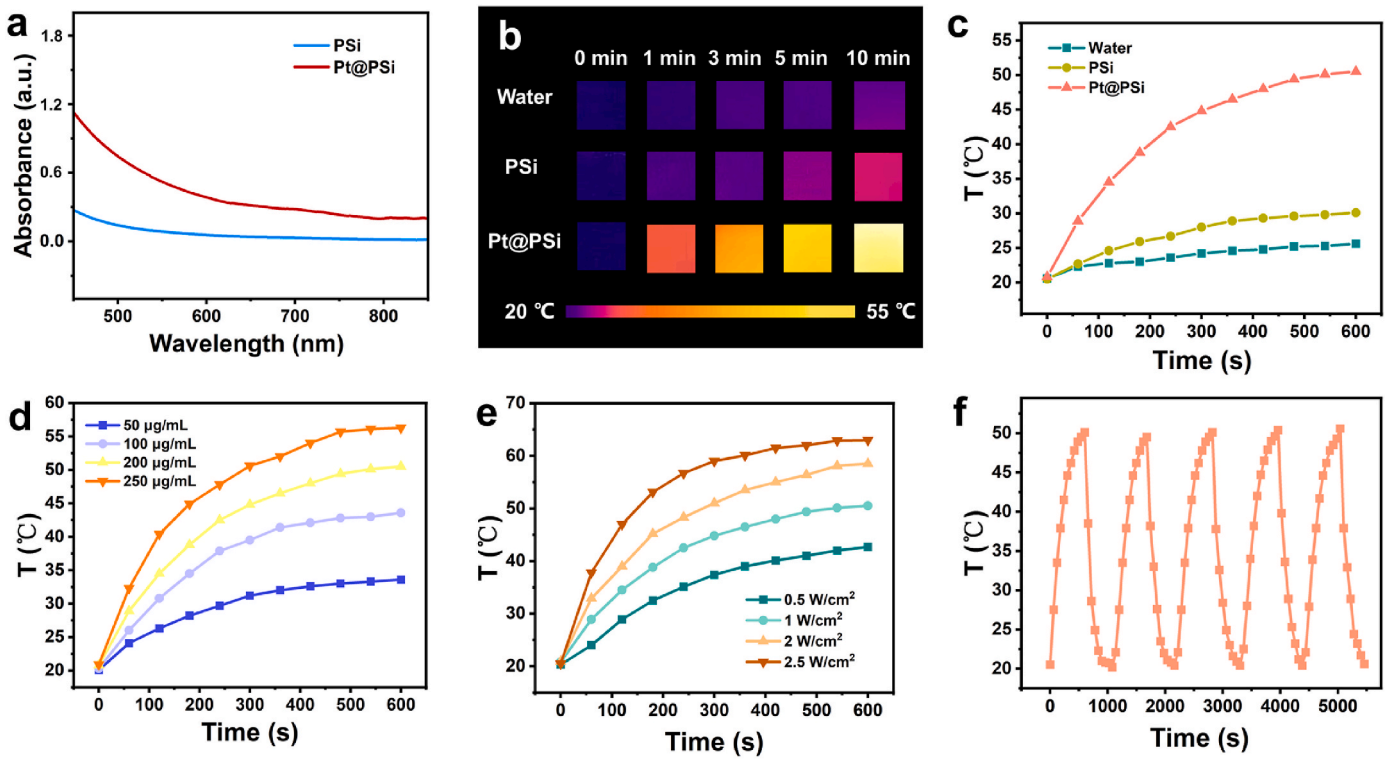

Fig. 2. Absorption and NIR photothermal properties of Pt@PSi nanocomposite. (a) Typical UV–vis absorption spectra of PSi NPs and Pt@PSi nanocomposites at a concentration of 200 μg/mL. Infrared thermal images (b) and relative photothermal curves (c) of water, PSi (200 μg/mL), Pt@PSi nanocomposites (200 μg/mL) irradiated with 808 nm NIR light (1 W/cm^2, 10 min). (d) The photothermal response curve of Pt@PSi nanocomposites irradiated with 808 nm NIR light (1 W/cm^2, 10 min) at different concentrations. (e) The photothermal response curve of Pt@PSi nanocomposites (200 μg/mL) irradiated with 808 nm NIR light (10 min) at different power intensities. (f) The photothermal stability curve of Pt@PSi nanocomposites (200 μg/mL) irradiated with 808 nm NIR light (1 W/cm^2, 10 min) over 5 cycles.

shown in Fig. 3a, the absorbance values of the reaction system do not change significantly in the blank and PSi groups due to the absence of enzyme or low catalytic activity of PSi. In contrast, the absorption of the Pt@PSi group changes significantly, with a characteristic absorption peak of oxidized TMB at 652 nm, proving that the catalytic reaction occurred. In addition, we find that the catalytic performance of the reaction system is further enhanced after 808 nm NIR laser irradiation. The reason for the above phenomenon may be attributed to the excitation of hot electrons on the Pt metallic surface under NIR light irradiation, leading to electron transfer and catalytic capacity enhancement [51]. On the other hand, the temperature increases of the reaction system due to the photothermal effect would also accelerate the kinetics of the catalytic reaction. As demonstrated in Fig. 3b, the catalytic reaction of Pt@PSi is fast, and the equilibrium state can be reached around 5 min. The irradiation of NIR laser significantly accelerates the catalytic process. To further confirm the catalytic reaction mechanism, ESR spectroscopy is used to further test the production of catalytic reaction process intermediates. The results in Fig. 3c show that the type of ROS produced by Pt@PSi-H_2O_2 system is ·OH with four 1:2:2:1 characteristic peak, regardless of whether it is under NIR light irradiation or not. However, under NIR light irradiation, Pt@PSi nanocomposites can produce more ·OH, suggesting that the material can provide more reactive radicals under NIR light stimulation, which further enhances the electron transfer and leads to the increase of catalytic activity.

On the basis of the above findings, we next performed steady-state kinetic analysis of the POD-like activity of Pt@PSi nanocomposites with or without NIR irradiation. As shown in Fig. 3d and e, the classical Michaelis-Menten curves and Lineweaver-Burk double reciprocal plots were obtained by varying the concentration of H_2O_2. Based on the data, common steady-state kinetic parameters of the enzyme including the Mie constant (K_m) and the maximum catalytic reaction rate (V_{max}) can be calculated and compared with other Pt-based nanozymes (Table S1). Typically, K_m represents the affinity of the POD-like enzyme for the H_2O_2 substrate, with smaller K_m representing higher affinity. V_{max} represents the catalytic efficiency, with higher V_{max} reflecting better catalytic activity. From the results, the Pt@PSi nanocomposites have comparable catalytic activity to other Pt nanozymes and even higher than common Pt NPs. The above phenomenon may be attributed to the fact that the nano-confinement effect of the PSi carrier can improve the selectivity of the catalytic reaction to the substrate and prevent the loss of reaction intermediates, which in turn improves the catalytic efficiency. It is worth noting that the synthesis of Pt@PSi nanocomposites does not require additional reducing and template agents, and thus has the characteristics of being greener, more economical and more efficient. In addition, NIR laser irradiation can further enhance the catalytic activity of the enzyme, which is consistent with the results above. Further, we find that the relative catalytic activity of the nanocomposites can indeed be increased with the rise of temperature, which can to some extent explain the increase of nanozyme activity by NIR laser (Fig. 3f). To further confirm this, the temperature of the nanocatalytic reaction is regulated to around 0 °C by using an ice water bath. As shown in Fig. S4, different laser densities and durations had no significant effect on the relative activity of the enzymatic catalytic reaction. Therefore, we believe that the enhancement of nanozyme activity by NIR light excitation mainly originates from the photothermal effect of the material. However, higher temperature than 60 °C may lead to inactivation of the enzyme. More importantly, the activity of the composites remains above 92 % after 14 days of storage at room temperature, proving the excellent storage stability of the Pt@PSi nanocomposites (Fig. 3g). Overall, the above results confirm the great potential of Pt@PSi smart materials as stimuli-responsive nanozymes.

As known, H_2O_2 and $\bullet O_2^-$ are the most abundant ROS produced in

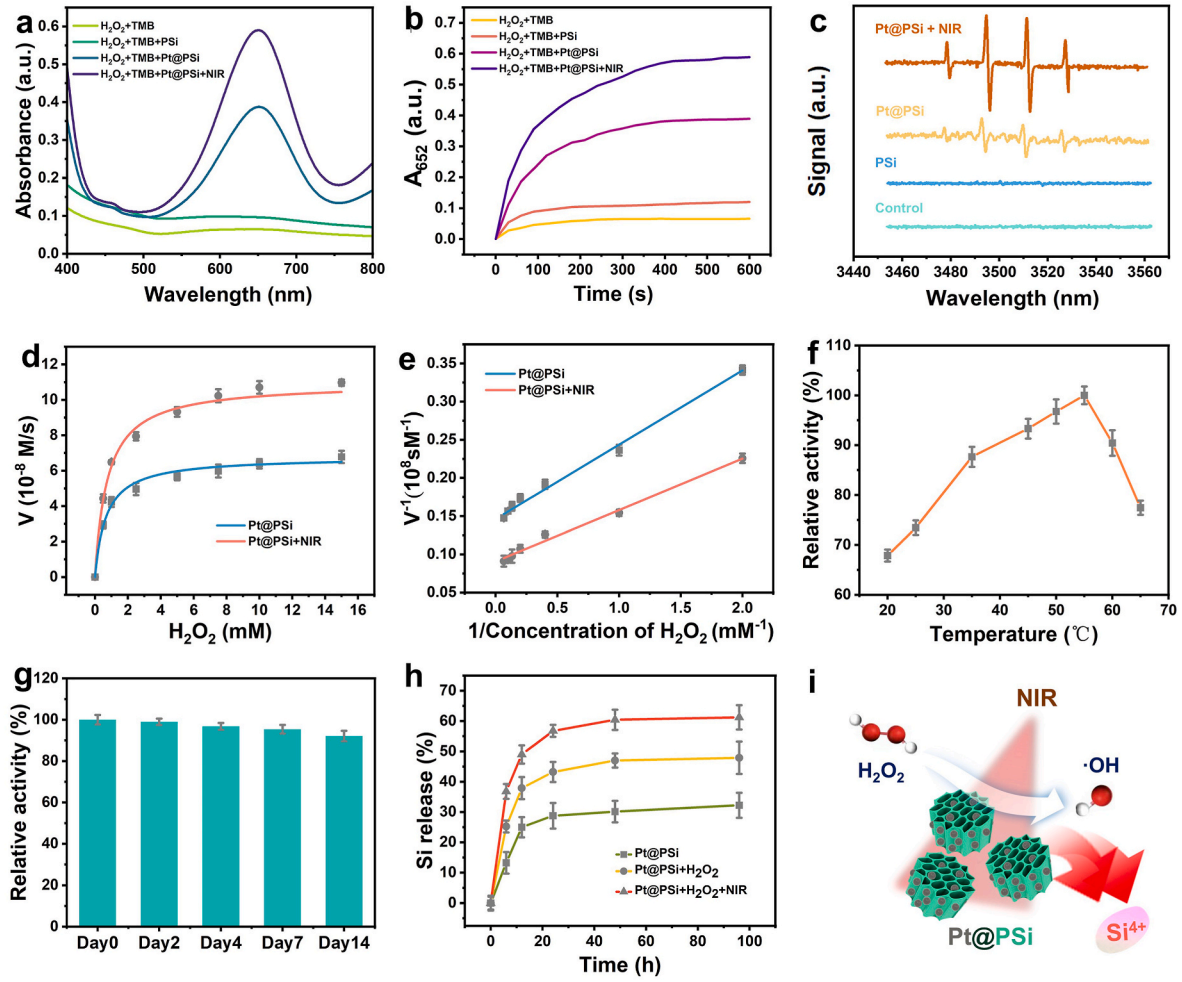

Fig. 3. (a) UV–vis absorbance spectra of different H_2O_2-TMB solutions added with blank, PSi, and Pt@PSi in the absence or presence of NIR light illumination after reaction for 10 min. (b) Time-dependent changes of the absorbance at 652 nm of H_2O_2-TMB solutions added with blank, PSi, and Pt@PSi in the absence or presence of NIR light illumination. (c) EPR spectra of the different reaction solutions demonstrating ·OH generation. The Michaelis-Menten kinetic profile (d) and Lineweaver-Burk plotting (e) for POD-like catalytic activity of Pt@PSi in the absence or presence of NIR light illumination using H_2O_2 as a substrate. (f) Changes in relative catalytic activity of the POD-like Pt@PSi nanocomposites at different temperatures (f) and storage time (g). (h) The release profile of Si^{4+} for different groups. (i) Schematic diagram of the NIR and nanozyme dual-driven Si release mechanism based on smart Pt@PSi nanocomposites.

cells during wound or injury [23,55]. Here, we compare the scavenging effects of different materials on H_2O_2 and $\bullet O_2^-$ at the same concentration (200 μg/mL). As shown in Fig. S5, Pt@PSi exhibited significantly enhanced scavenging ability for both types of ROS compared to PSi, which may be attributed to the ROS scavenging effect of Pt nanozyme. Additionally, the ROS scavenging ability was further enhanced after NIR laser treatment, which may be attributed to the photothermal effect enhancing the Pt-mediated ROS scavenging capability, consistent with previous reports [56,57].

A key focus of this work is to exploit PSi degradation activity for efficient bioactive ion release and pro-angiogenesis therapy. Owing to the excellent photothermal and POD-like activities of the Pt@PSi nanocomposites, it is reasonable to speculate that these two properties will endow the smart nanocomposites with stimuli-responsive ion release behaviors. As shown in Fig. 3h, both H_2O_2 and NIR light stimulation significantly accelerate the degradation of PSi and thus the release of silicon ions. The promotion effect is further enhanced by the combination of the two factors. The reason for the above phenomenon is that PSi is an oxidation-induced degradation material and the degradation of PSi is also heat-sensitive [40]. Accordingly, we propose a novel PSi-based therapeutic strategy in which ROS generated by nanozyme-catalyzed H_2O_2 and heat generated by NIR laser illumination can be used as a dual stimulus to drive PSi degradation and on-demand ion release, which has a promising application in pro-angiogenesis treatment of wounds (Fig. 3i).

3.3. *In vitro antibacterial and antibiofilm effect exploration*

Encouraged by the excellent photothermal and POD-like activities of Pt@PSi nanocomposites, we subsequently investigated the *in vitro* antibacterial effect using *S. aureus* as a test model. *S. aureus* was treated with different materials in the culture medium respectively. Then, *S. aureus* in different groups continued to be cultured and the optical density was recorded. As shown in Fig. 4a, the PSi NPs have nearly no inhibitory effect on bacterial growth regardless of NIR laser irradiation due to the lack of photothermal and catalytic activity. However, the Pt@PSi nanocomposites exhibit good bactericidal effects, and can almost completely inhibit bacterial growth after NIR laser irradiation over an 8-h period. Fig. 4b shows that the synergistic therapy based on Pt@PSi nanocomposites can significantly increase the bactericidal effect and decrease the bacterial survival rate. With the help of 808 nm NIR laser (1.0 W/cm^2), the bacterial viablity after Pt@PSi treatment is only 4.8 %, which is much lower than that of single nanozyme catalytic therapy (63.7 %). In addition, the plate counting method is used to determine the viable bacteria in each group after treatment, and the results are similar to the above results (Fig. 4c). In addition, SEM is used

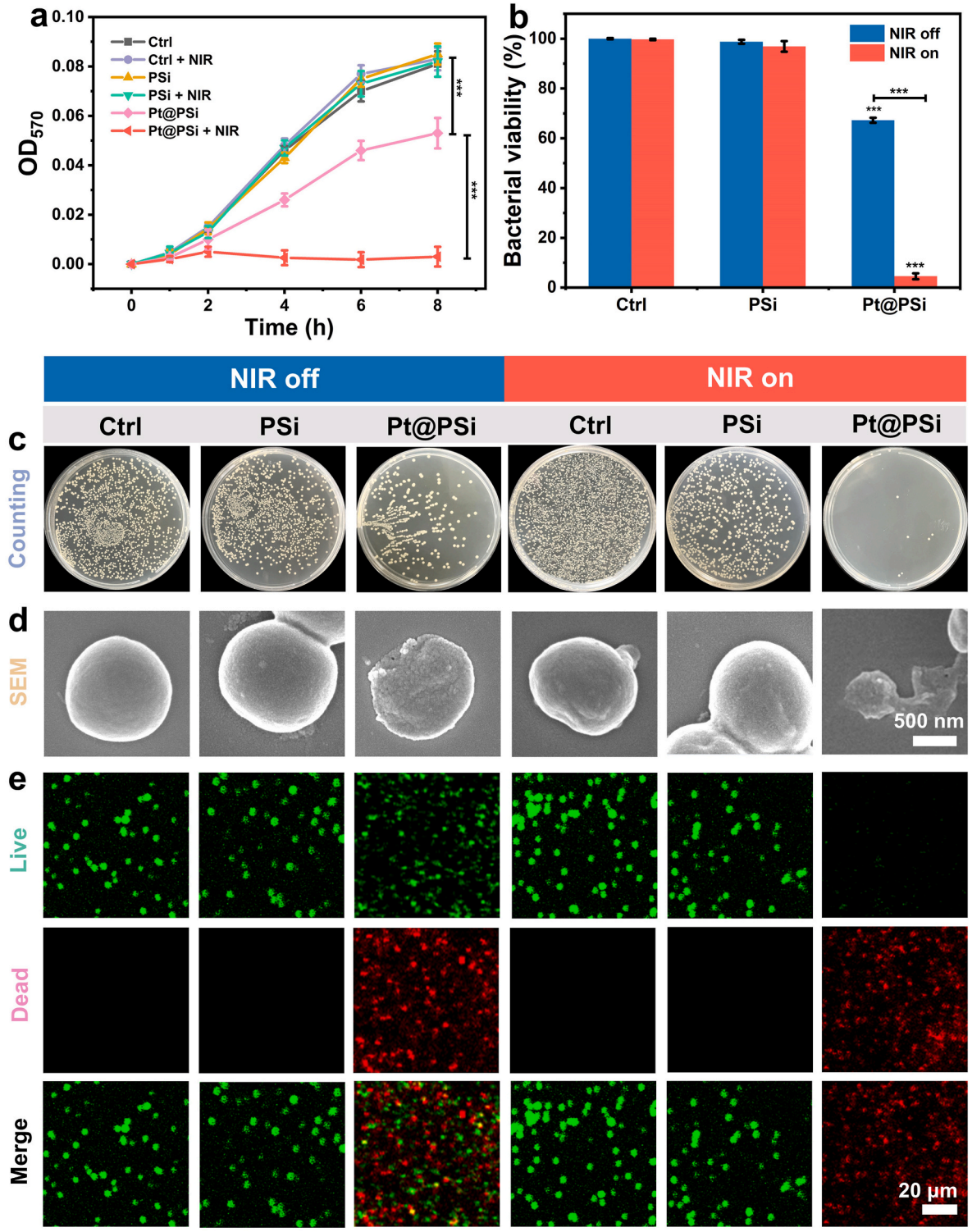

Fig. 4. (a) Real-time optical density values for *S. aureus* after treatment with PBS (Ctrl), PSi, and Pt-PSi in the absence or presence of 808 nm NIR light illumination (1 W/cm^2, 10 min), respectively. (b) Bacterial viabilities of *S. aureus* after treatment with PBS (Ctrl), PSi, and Pt-PSi in the absence or presence of 808 nm NIR light illumination (1 W/cm^2, 10 min), respectively. The data are presented as mean ± SD, $n = 3$, $^{***}p < 0.001$. (c) Colonies counting photographs of *S. aureus* grown on agar plates after treatment with PBS (Ctrl), PSi, and Pt-PSi in the absence or presence of 808 nm NIR light illumination (1 W/cm^2, 10 min), respectively. (d) SEM morphological images of typical *S. aureus* cells after treatment with PBS (Ctrl), PSi, and Pt-PSi in the absence or presence of 808 nm NIR light illumination (1 W/cm^2, 10 min), respectively. (e) Fluorescence images of *S. aureus* cells stained with SYTO 9/PI after treatment with PBS (Ctrl), PSi, and Pt-PSi in the absence or presence of 808 nm NIR light illumination (1 W/cm^2, 10 min), respectively.

to observe the morphology of bacteria in each group after treatment. As shown in Fig. 4d, the *S. aureus* cells exhibit a full and rounded state in the four groups of Ctrl, Ctrl + NIR, PSi, PSi + NIR, which proves high viability. In contrast, the bacteria in the Pt@PSi and Pt@PSi + NIR groups gradually undergo cell lysis and collapse. Then, SYTO9 and PI dyes are used to analyze the bacterial cells after different treatments by live/dead bacterial staining assay. As shown in Fig. 4e, the Ctrl and PSi groups show bright green fluorescence (live bacteria) regardless of the presence or absence of NIR laser, indicating similar negligible antibacterial effects. However, the Pt@PSi group strains show significantly higher red fluorescence, but still has some live bacteria. Not surprisingly, the treatment groups of Pt@PSi exhibit significantly enhanced red fluorescence and negligible green fluorescence when exposed to NIR laser. The above results validate the efficient antibacterial performance of the combination therapy in several ways.

In burn wound infections, the presence of biofilms is often observed, which enhances the antibiotic resistance of bacteria, making the infection difficult to control and delaying the wound healing process [43,53]. To address this issue, we investigate the antibiofilm capabilities of different groups. As shown in Fig. S6a, the remaining biofilm (%) after treatment with each group was quantified and calculated using the crystal violet staining method. The results indicate that the combined therapy can effectively eliminate the biofilm, with less than 5 % remaining. Further confirmation is provided by live-dead fluorescence staining of the remaining biofilm, which shows that the biofilm activity in the combined therapy group is the lowest, with virtually no green fluorescence from viable bacteria observed (Fig. S6b). These results demonstrate that the proposed strategy is an effective intervention for biofilms, potentially further improving the treatment outcomes for burn infections.

3.4. *In vitro* cytocompatibility, ROS scavenging, and migration effect evaluation

Next, we test the *in vitro* cytocompatibility of the smart nanocomposite. The blood compatibility of Pt@PSi composite is first investigated by incubating the composite with RBCs at different concentrations. As shown in Fig. 5a, the calculated hemolysis rate is less than 3 % regardless of the NIR laser irradiation, indicating that the Pt@PSi nanocomposites did not produce hemolysis when exposed to blood. Further, *in vitro* cytotoxicity of Pt@PSi nanocomposites is studied on HUVECS using CellTiter-Lumi reagent after incubation with different concentrations of materials for 48 h, respectively. As indicated in Fig. 5b, when 500 μg/mL of Pt@PSi nanocomposites is used alone, cell viability remains at 92.4 %, indicating low cytotoxicity. Further NIR laser treatment of Pt@PSi nanocomposites cannot reduce HUVEC cell viability significantly. The good cytocompatibility of the Pt@PSi nanocomposites may be attributed to the fact that the loading of metallic nanomaterials in PSi can reduce the contact probability with the cells, and then reduce their cytotoxicity [43].

Pt nanozymes are proven to exhibit good ROS scavenging activity through various redox pathways [58]. Hence, Pt@PSi nanozyme is expected to modulate the over-expressed ROS in damaged cells. To evaluate the ROS scavenging capability of materials *in vitro*, the intracellular levels of ROS after treatment with different groups were assessed using DCFH-DA staining. As shown in Fig. S7, compared to the control group, PSi had little effect on the green fluorescence signal of the DCFH-DA probe for ROS. However, the ROS level was efficiently decreased in

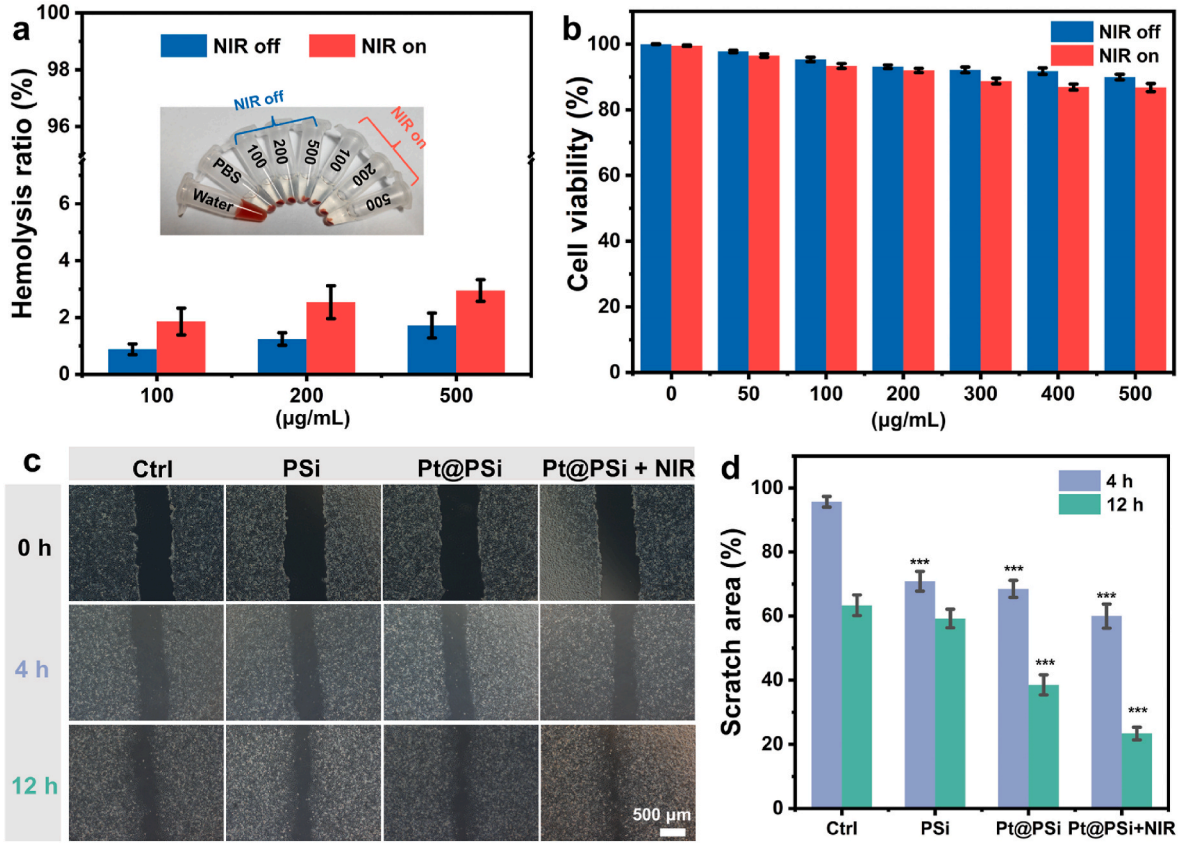

Fig. 5. (a) Blood compatibility of RBCs after coincubation with Pt-PSi nanocomposites at different concentrations for 48 h. In the NIR on group, Pt-PSi nanocomposites was irradiated with 808 nm NIR light (1 W/cm^2, 10 min). (b) Cell viabilities of HUVECs after coincubation with Pt-PSi nanocomposites at different concentrations for 48 h. In the NIR on group, Pt-PSi nanocomposites was irradiated with 808 nm NIR light (1 W/cm^2, 10 min). *In vitro* wound-healing assay results including the microscopy images (c) and the scratch area quantification (d) of HUVECs after coincubation with PBS (Ctrl), PSi, Pt-PSi, and Pt + NIR for 4 h and 12 h. The data are presented as mean ± SD, $n = 3$, $^*p < 0.05$, $^{**}p < 0.01$, and $^{***}p < 0.001$.

intracellular samples after Pt@PSi treatment, demonstrating its great potential for wound healing.

In our previous studies, PSi can effectively promote the migration of HUVECS due to the release of Si ions, thereby contributing to wound healing [37,43]. However, owing to the relatively slow degradation of Si ions, significant healing results require milligram doses. Encouraged by the on-demand release of Si ions *in vitro*, we hypothesize that the NIR laser and nanozyme dual-driven nanocomposites can significantly accelerate the cell migration at a lower concentration. Here, we investigate the effect of different treatments on cell migration by standard scratch test. After incubation for 4 h and 12 h in the incubator, HUVECs were photographed and the area of the scratch area at different time

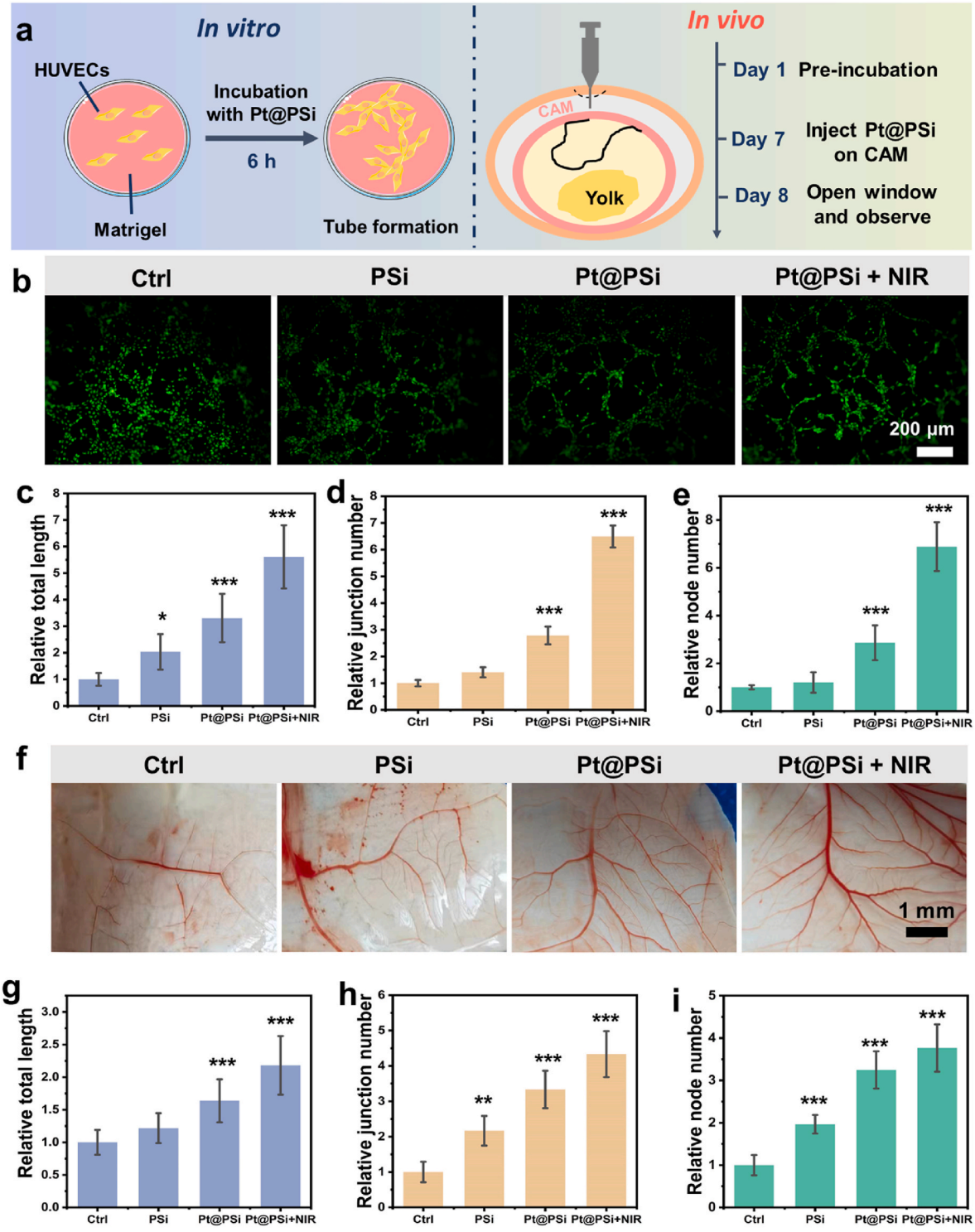

Fig. 6. (a) Schematic diagram of process of *in vitro* tube formation experiment for HUVECs and *in vitro* CAM assay. (b) Fluorescence images for *in vitro* tube formation of HUVECs stained with Calcein-AM after treatment with PBS (Ctrl), PSi, and Pt-PSi in the absence or presence of 808 nm NIR light illumination (1 W/cm^2, 10 min), respectively. Relative quantitative analysis of total length (c), junction number (d), and node number (e) in tube formation assay. (f) Photographs for *in vivo* CAM model at Day 8 after treatment with PBS (Ctrl), PSi, and Pt-PSi in the absence or presence of 808 nm NIR light illumination (1 W/cm^2, 10 min), respectively. Relative quantitative analysis of total length (g), junction number (h), and node number (i) in CAM model. The data are presented as mean ± SD, $n = 3$, ***$p < 0.001$.

points was analyzed with ImageJ software. As shown in Fig. 5c and d, the scratch area of PSi group increases slightly compared with the Ctrl group. However, after treatment with Pt@PSi and Pt@PSi + NIR groups at a concentration of 500 μg/mL, the scratch area of the cells is further reduced due to the faster release of Si ions. After 12 h, the Pt@PSi + NIR group decreases significantly to 22.7 %, which is much smaller than the group without NIR (35.9 %). These results suggest that the degradation strategy mediated by NIR laser and nanozyme can effectively amplify the ability of promoting cell migration.

3.5. *In vitro tube formation and in vivo angiogenesis test*

It is well known that angiogenesis is the key process during the wound healing [37]. However, burn wounds often fail to rebuild the vascular spontaneously because of severe tissue damage [4]. Specifically, the Si ions released from PSi particles trigger an upregulation in the expression of VEGF, kinase insert domain-containing receptor (KDR) and HIF-1α expression in HUVECs [37]. Because of the powerful role of Si element in promoting angiogenesis, here we explore the pro-angiogenic activity of the novel PSi-based nanozyme. As shown in Fig. 6a, the effect of the composite on angiogenesis is explored *in vitro* and *in vivo* using the mature Matrigel matrix tube formation experiment and CAM experiment, respectively. As shown in Fig. 6b, tube formation in the material-treated group becomes more pronounced from the fluorescence images of the cells after incubation of 4 h on Matrigel.

Next, ImageJ software was used to quantitatively analyze the tube formation by the image with the Ctrl group set to 1. As shown in Fig. 6c–e, some of the key parameters of angiogenesis, such as total length, junction number, and node number, are significantly improved after treatment with dual-driven smart nanocomposites compared with other groups. The above results indicate that our proposed strategy based on Pt@PSi nanozyme has a significant promotion on HUVEC tube formation ability. In addition, to further investigate the effect of materials on angiogenesis *in vivo*, we perform a CAM experiment in a chicken embryo model. After 1 day of incubation with materials, the changes of blood vessels formed on CAM were recorded with a camera. As shown in Fig. 6f, angiogenesis level is significantly improved in the PSi, Pt@PSi, and Pt@PSi + NIR groups compared with the Ctrl group. The Pt@PSi + NIR group has the most obvious branching vessels, indicating a high degree of vascular maturity. This conclusion is also supported by the

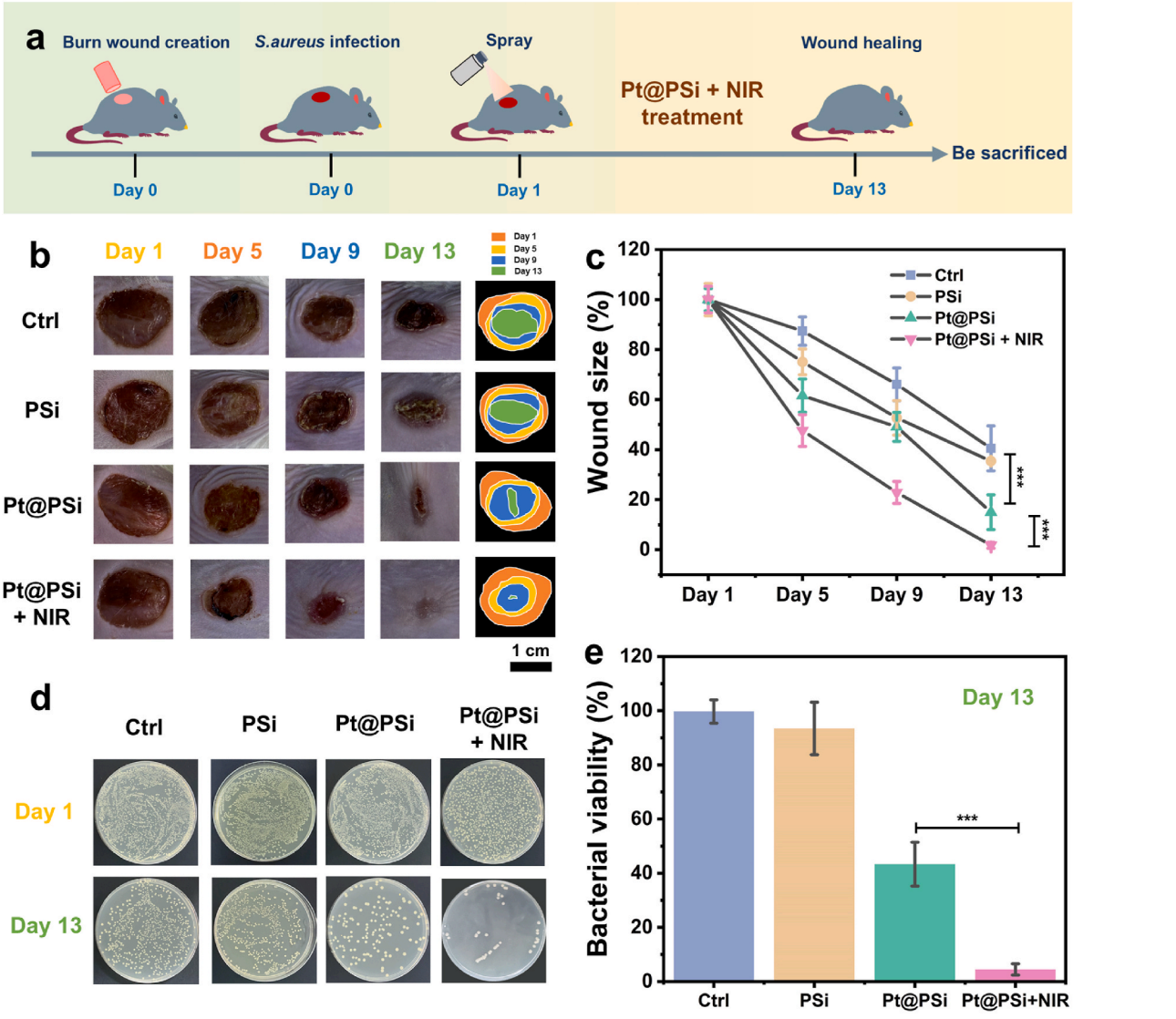

Fig. 7. (a) Schematic illustration of the whole process for the *in vivo* animal experiment. (b) The wound healing photographs the burn infected wounds after different treatments at Day 1, Day 5, Day 9 and Day 13. (c) Wound size change of the burn infected wounds after different treatments at set time points. (d) The bacterial colonies photographs of *S.aureus* collected from the skin wound tissues at Day 1 and Day 13 and (e) the corresponding bacterial viabilities after different treatments at Day 13. The data are presented as mean ± SD, $n = 5$, $^{***}p < 0.001$.

quantitative analysis of the relevant parameters in Fig. 6g–i. In conclusion, both *in vitro* and *in vivo* experiments further confirm that dual-driven Pt@PSi bioactive material can effectively promote angiogenesis.

3.6. In vivo burn infected wound healing and histopathological analysis

After demonstrating the great potential of Pt@PSi nanocomposites for bacterial killing, cell regulation, and angiogenesis *in vitro*, we then established a full-thickness skin burn infection model to evaluate the integrated wound-healing properties of the smart nanomaterials *in vivo*. As shown in Fig. 7a, an animal model of refractory burn infection was established by first heating the wound with an electric heating rod followed by *S. aureus* infection. The different NPs were then evenly applied to the wound. The Pt@PSi + NIR group was performed by irradiation of nanocomposites with NIR light for 5 min every other day. To investigate the *in vivo* photothermal properties of Pt@PSi, thermal imager was used to record the wound temperature changes after 5 min exposure to the 808 nm NIR laser. Compared with the other groups, the wound temperature of Pt@PSi group increases to 49.1 °C, while that of PBS and PSi group increased only slightly, indicating that the nanocomposites have good photothermal properties *in vivo* (Fig. S8). As shown in Fig. 7b and c, photos of wounds during the healing process are recorded on Day 1, 5, 9, and 13, and the wound size changes are analyzed by ImageJ software. Because no treatment is applied, the wound area in the Ctrl group remained above 40 % of the original area after 13 days, indicating the difficult-healing characteristics of the burn infected wounds. Besides, the wound healing is not improved obviously after PSi treatment. As a comparison, the Pt@PSi and Pt@PSi + NIR groups show better results in accelerating wound healing than the other groups. In particular, wound size after treatment is significantly smaller in the Pt@PSi + NIR group than in the other groups at multiple time points and the wounds is almost completely healed on Day 13. These results suggest that dual-

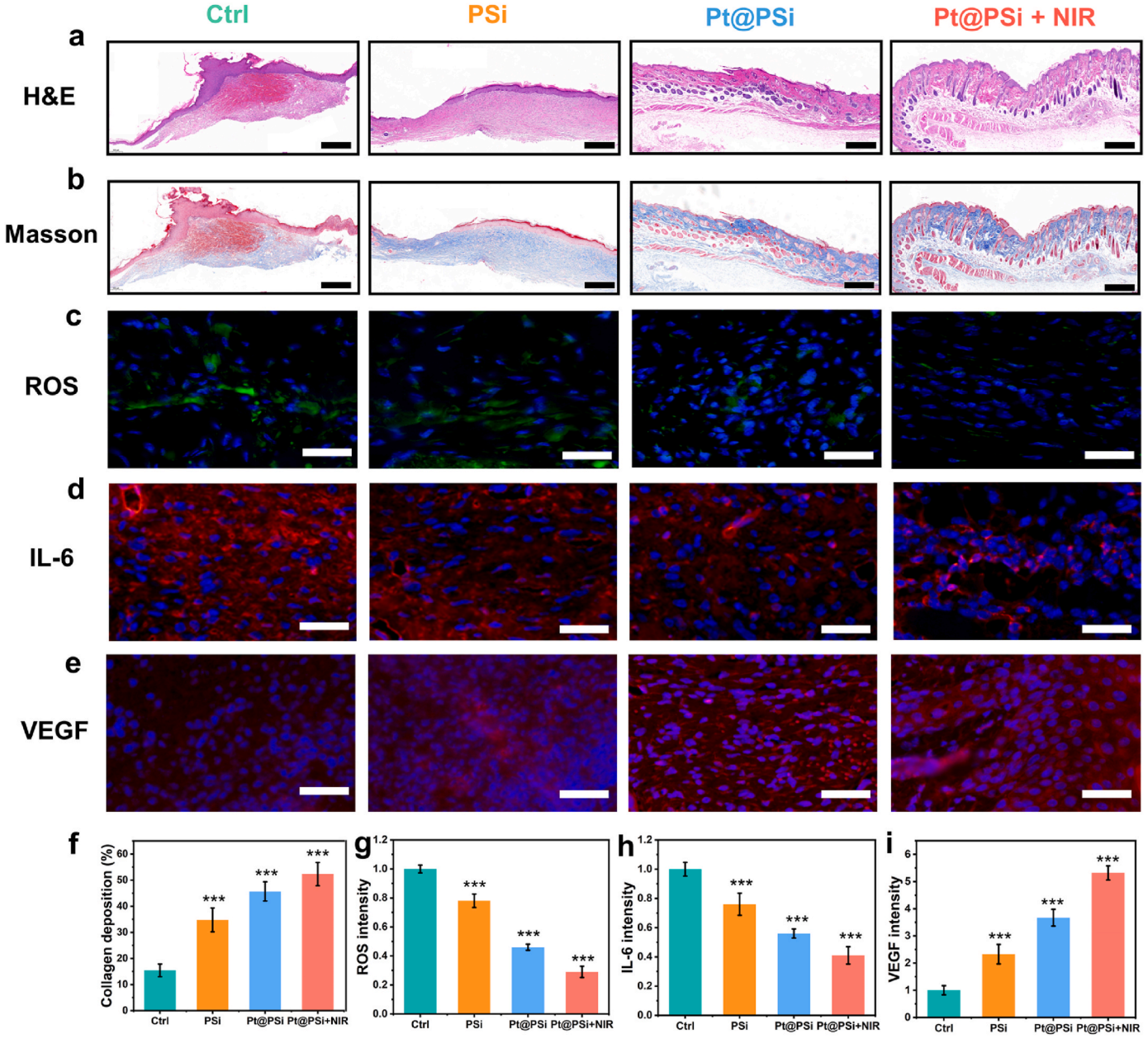

Fig. 8. H&E (a) and Masson (b) staining images of skin wound tissues at Day 13, Scale bar: 50 μm. Immunofluorescence staining images of ROS (c), IL-6 (d) and VEGF (e) in skin wound tissue at Day 13, Scale bar: 50 μm. Relative quantitative analysis of collagen deposition (f), ROS intensity (g), IL-6 intensity (h), and VEGFintensity (i) skin wound tissue at Day 13. The data are presented as mean ± SD, $n = 3$, $^{***}p < 0.001$.

driven Pt@PSi nanotherapy has excellent acceleration properties in wound healing *in vivo*. In addition, plate counts and corresponding viability analysis of bacteria from wounds on Day 1 and Day 13 reveal a significant reduction in bacterial colonies in the Pt@PSi + NIR treatment group (Fig. 7d and e). The viability of bacteria after treatment is only 4.3 %, showing that Pt@PSi + NIR group has excellent antibacterial activity *in vivo*. Moreover, the weight of the mice in each group do not change much during treatment, suggesting that the effects of these treatments on mouse growth were negligible (Fig. S9).

Further, to assess the quality of wound healing after different treatments, hematoxylin-eosin staining (H&E) and Masson trichrome staining were performed on the treated skin tissues of each group. As shown in Fig. 8a and b, the histological results show significant differences between the groups, which are consistent with wound healing. From the H&E staining, extensive areas of deep red are observed in the Ctrl group, which is a significant characteristic of severe skin damage, supporting a high degree of tissue breakdown with little healing property. Besides, the PSi group also has a relatively low quality of healing with a high degree of inflammatory infiltration. Skin tissues treated with Pt@PSi and Pt@PSi + NIR groups reveal more blood vessels as well as appendages such as hair follicles, suggesting the potential of the proposed combination therapy to promote tissue remodeling. Therefore, from a pathological perspective, the wound healing efficacy is ranked as follows: Pt@PSi + NIR > Pt@PSi > PSi > Ctrl, which is consistent with the experimental results of wound healing. During wound healing, metabolic deposition of collagen is associated with tissue remodeling, representing the healing quality of the skin. Hence, collagen deposition is assessed by Masson staining analysis. As shown in Fig. 8f, collagen deposition in Pt@PSi + NIR group is the highest among the groups. The results of the histological analysis suggest that the combination nanotherapy has the best therapeutic effect in burn-infected wound healing.

To explore the ROS regulation and anti-inflammatory capacity of the combination therapy, ROS and IL-6 expression levels in the skin tissue were assessed by histofluorescence staining. As shown in Fig. 8c and d, the ROS (green) and IL-6 (red) signals in the Pt@PSi + NIR group are much lower than those in the control and other treatment groups. Further quantitative analysis shows that the composite nanozymes have excellent *in vivo* ROS scavenging and anti-inflammatory effects (Fig. 8g and h). This conclusion is also aided by the changes in the serum levels of inflammatory factor (IL-6 and TNF-α) in different groups after treatment (Fig. S10). Blood vessels can provide a source of nutrients and oxygen for new granulation tissue growth and epithelial regeneration, and are also critical for improving the quality of wound healing. Therefore, we perform immunofluorescence staining and analysis of VEGF expression. As indicated in Fig. 8e, the expression of VEGF in skin tissues after treatment with various PSi-based materials is significantly higher than that in the Ctrl group, especially the highest intensity is found in the Pt@PSi + NIR group. The above results are consistent with the aforementioned *in vitro* tube-forming experiments that dual-driven PSi-based nanozymes are favorable therapeutic platforms for angiogenesis.

Next, the blood biosafety of the different treatment was tested. As shown in Fig. S11, common blood biochemicals, including white blood cells (WBCs), RBCs, platelets (PLT), and hemoglobin (HGB), are within the normal range after Pt@PSi + NIR treatment. In addition, the treatment group do not induce abnormal changes in liver and kidney function indicators such as glutamate aminotransferase (ALT), alanine aminotransferase (AST), urea, uric acid (UA), creatinine (CREA) and blood urea nitrogen (BUN) (Fig. S12). Finally, the *in vivo* biosafety of the composite materials was further assessed by H&E staining of major organs (heart, liver, spleen, lungs and kidneys) in mice, and no significant pathological damage is observed after Pt@PSi + NIR treatment compared to the Ctrl group (Fig. S13). The above results indicate good biocompatibility of our novel therapeutic platform. Moreover, the photothermal temperature of Pt@PSi-based therapy can be easily adjusted by varying the material dosage, laser power density, and irradiation time (Fig. 2). Hence, by adjusting the laser irradiation time, laser wavelength (extending to the NIR II window), and laser power density, the treatment effect can be optimized and damage to normal tissues can be minimized for future application.

4. Conclusion

In the present work, we prepare Pt@PSi nanocomposites with multiple bioactivities for synergistic treatment of burn infected wounds through a simple and efficient confinement synthesis strategy. The Pt@PSi smart nanocomposites exhibit excellent NIR photothermal conversion activity and POD-like property, which enabled the combined PTT and nanocatalytic therapy for antibacterial treatment. Notably, compared to conventional nanozymes, the Pt@PSi nanocomposites also present bioactivities that promoted cell migration, tube formation and vascularization owing to the release of Si ions dual-driven by both the NIR light and Pt nanozyme. The established stimuli-responsive pro-angiogenetic nanozymes exhibit excellent pro-healing properties by eliminating inflammation, inhibiting bacteria and promoting angiogenesis in burn infected wound model *in vivo*. In conclusion, the Pt@PSi smart nanocomposites provide a novel strategy for high-quality repair of damaged tissues in burn patients suffering from bacterial infections. Thanks to the simple preparation method and multiple bioactivities of the composites, we believe that this therapeutic strategy will be effectively expanded to the efficient treatment of other chronic infectious diseases in future.

CRediT authorship contribution statement

Wei Duan: Writing – original draft, Visualization, Validation, Supervision, Software, Resources, Project administration, Methodology, Investigation, Funding acquisition, Formal analysis, Data curation, Conceptualization. **Yue Gao:** Visualization, Validation, Software, Methodology, Investigation, Formal analysis. **Ruru Xu:** Resources, Methodology, Investigation, Formal analysis, Data curation. **Sheng Huang:** Validation, Methodology, Investigation, Formal analysis, Data curation. **Xueqian Xia:** Software, Methodology, Investigation, Formal analysis, Data curation. **Jingwen Zhao:** Visualization, Validation, Software, Investigation, Data curation. **Longhuan Zeng:** Methodology, Investigation, Formal analysis, Data curation. **Qiaolin Wei:** Supervision, Software, Methodology, Funding acquisition. **Jia-Wei Shen:** Writing – review & editing, Supervision, Resources, Investigation, Funding acquisition, Data curation, Conceptualization. **Jianmin Wu:** Writing – review & editing, Visualization, Supervision, Resources, Project administration, Methodology, Investigation, Funding acquisition, Data curation, Conceptualization. **Yongke Zheng:** Writing – review & editing, Visualization, Validation, Supervision, Software, Resources, Project administration, Methodology, Investigation, Funding acquisition, Formal analysis, Conceptualization.

Declaration of competing interest

The authors declare that they have no known competing financial interests or personal relationships that could have appeared to influence the work reported in this paper.

Acknowledgments

This work was financially supported by the National Natural Science Foundation of China (Nos. 32401103, 22378090, 82303809), the Zhejiang Provincial Natural Science Foundation of China (No. LQN25H180009), the Medical Science and Technology Project of Zhejiang Province (No. 2025KY179), the Visiting Scholar Fund of State Key Laboratory of Silicon and Advanced Semiconductor Materials (No. SKL2024-01), and the Interdisciplinary Research Project of Hangzhou Normal University (No. 2024JCXK02).

Appendix A. Supplementary data

Supplementary data to this article can be found online at https://doi.org/10.1016/j.mtbio.2025.101522.

Data availability

Data will be made available on request.

References

[1] M.G. Jeschke, M.E. van Baar, M.A. Choudhry, K.K. Chung, N.S. Gibran, S. Logsetty, Burn injury, Nat. Rev. Dis. Prim. 6 (1) (2020) 11.

[2] S. Li, K. Pang, S. Zhu, K. Pate, J. Yin, Perfluorodecalin-based oxygenated emulsion as a topical treatment for chemical burn to the eye, Nat. Commun. 13 (1) (2022) 7371.

[3] Y. Wang, J. Beekman, J. Hew, S. Jackson, A.C. Issler-Fisher, R. Parungao, S. S. Lajevardi, Z. Li, P.K. Maitz, Burn injury: challenges and advances in burn wound healing, infection, pain and scarring, Adv. Drug Deliv. Rev. 123 (2018) 3–17.

[4] M.M. Rybarczyk, J.M. Schafer, C.M. Elm, S. Sarvepalli, P.A. Vaswani, K.S. Balhara, L.C. Carlson, G.A. Jacquet, Prevention of burn injuries in low-and middle-income countries: a systematic review, Burns 42 (6) (2016) 1183–1192.

[5] Y. Yuan, S. Shen, D. Fan, A physicochemical double cross-linked multifunctional hydrogel for dynamic burn wound healing: shape adaptability, injectable self-healing property and enhanced adhesion, Biomaterials 276 (2021) 120838.

[6] J. Lan, L. Shi, W. Xiao, X. Zhang, S. Wang, A rapid self-pumping organohydrogel dressing with hydrophilic fractal microchannels to promote burn wound healing, Adv. Mater. 35 (38) (2023) 2301765.

[7] S. Wang, S. Wu, Y. Yang, J. Zhang, Y. Wang, R. Zhang, L. Yang, Versatile hydrogel dressings that dynamically regulate the healing of infected deep burn wounds, Adv. Healthcare Mater. 12 (30) (2023) 2301224.

[8] M. Zhao, M. Kang, J. Wang, R. Yang, X. Zhong, Q. Xie, S. Zhou, Z. Zhang, J. Zheng, Y. Zhang, Stem cell-derived nanovesicles embedded in dual-layered hydrogel for programmed ROS regulation and comprehensive tissue regeneration in burn wound healing, Adv. Mater. (2024) 2401369.

[9] Y. Huang, L. Mu, X. Zhao, Y. Han, B. Guo, Bacterial growth-induced tobramycin smart release self-healing hydrogel for Pseudomonas aeruginosa-infected burn wound healing, ACS Nano 16 (8) (2022) 13022–13036.

[10] H. Zhang, X. Yang, Y. Huang, Y. Li, Q. Hu, Q. Wei, W. Xu, W. Ding, Y. Guo, J.-W. Shen, Reviving intervertebral discs: treating degeneration using advanced delivery systems, Mol. Pharm. 21 (2) (2024) 373–392.

[11] X. Ji, Z. Tang, H. Liu, Y. Kang, L. Chen, J. Dong, W. Chen, N. Kong, W. Tao, T. Xie, Nanoheterojunction-mediated thermoelectric strategy for cancer surgical adjuvant treatment and β-Elemene combination therapy, Adv. Mater. 35 (8) (2023) 2207391.

[12] M. Wang, X. Huang, H. Zheng, Y. Tang, K. Zeng, L. Shao, L. Li, Nanomaterials applied in wound healing: mechanisms, limitations and perspectives, J. Contr. Release 337 (2021) 236–247.

[13] T. Liu, Y. Lu, R. Zhan, W. Qian, G. Luo, Nanomaterials and nanomaterials-based drug delivery to promote cutaneous wound healing, Adv. Drug Deliv. Rev. 193 (2023) 114670.

[14] W. Duan, K. Xu, S. Huang, Y. Gao, Y. Guo, Q. Shen, Q. Wei, W. Zheng, Q. Hu, J.-W. Shen, Nanomaterials-incorporated polymeric microneedles for wound healing applications, Int. J. Pharm. (2024) 124247.

[15] L. He, D. Di, X. Chu, X. Liu, Z. Wang, J. Lu, S. Wang, Q. Zhao, Photothermal antibacterial materials to promote wound healing, J. Contr. Release 363 (2023) 180–200.

[16] H. Chen, L. Wu, T. Wang, F. Zhang, J. Song, J. Fu, X. Kong, J. Shi, PTT/PDT-induced microbial apoptosis and wound healing depend on immune activation and macrophage phenotype transformation, Acta Biomater. 167 (2023) 489–505.

[17] X. Zhao, Z. Chen, S. Zhang, Z. Hu, J. Shan, M. Wang, X.-L. Chen, X. Wang, Application of metal-organic frameworks in infectious wound healing, J. Nanobiotechnol. 22 (1) (2024) 387.

[18] W. Huang, P. Xu, X. Fu, J. Yang, W. Jing, Y. Cai, Y. Zhou, R. Tao, Z. Yang, Functional molecule-mediated assembled copper nanozymes for diabetic wound healing, J. Nanobiotechnol. 21 (1) (2023) 294.

[19] M. Du, X. He, D. Wang, Z. Jiang, X. Zhao, J. Shen, An NIR-II-enhanced nanozyme to promote wound healing in methicillin-resistant Staphylococcus aureus infections, Acta Biomater. 179 (2024) 300–312.

[20] X. Wang, X. Sun, T. Bu, Q. Wang, H. Zhang, P. Jia, L. Li, L. Wang, Construction of a photothermal hydrogel platform with two-dimensional PEG@ zirconium-ferrocene MOF nanozymes for rapid tissue repair of bacteria-infected wounds, Acta Biomater. 135 (2021) 342–355.

[21] B. Xu, H. Wang, W. Wang, L. Gao, S. Li, X. Pan, H. Wang, H. Yang, X. Meng, Q. Wu, A single-atom nanozyme for wound disinfection applications, Angew. Chem. 131 (15) (2019) 4965–4970.

[22] C. Liu, X. Zhao, Z. Wang, Y. Zhao, R. Li, X. Chen, H. Chen, M. Wan, X. Wang, Metal-organic framework-modulated Fe3O4 composite au nanoparticles for antibacterial wound healing via synergistic peroxidase-like nanozymatic catalysis, J. Nanobiotechnol. 21 (1) (2023) 427.

[23] L. Chen, S. Xing, Y. Lei, Q. Chen, Z. Zou, K. Quan, Z. Qing, J. Liu, R. Yang, A glucose-powered activatable nanozyme breaking pH and H_2O_2 limitations for treating diabetic infections, Angew. Chem. 133 (44) (2021) 23726–23731.

[24] X. Zhao, Y. Chen, R. Niu, Y. Tang, Y. Chen, H. Su, Z. Yang, X. Jing, H. Guan, R. Gao, NIR plasmonic nanozymes: synergistic enhancement mechanism and multi-modal anti-infection applications of MXene/MOFs, Adv. Mater. 36 (8) (2024) 2307839.

[25] L. Li, D. Wang, L. Ren, T. Wang, X. Tan, F. Cui, T. Li, J. Li, Chitosan-chelated carbon dots-based nanozyme of extreme stability with super peroxidase activity and antibacterial ability for wound healing, Int. J. Biol. Macromol. 258 (2024) 129098.

[26] Q. Li, M. Dong, Q. Han, Y. Zhang, D. Yang, D. Wei, Y. Yang, Enhancing diabetic wound healing with a pH-responsive nanozyme hydrogel featuring multi-enzyme-like activities and oxygen self-supply, J. Contr. Release 365 (2024) 905–918.

[27] L. Ye, X. He, E. Obeng, D. Wang, D. Zheng, T. Shen, J. Shen, R. Hu, H. Deng, The CuO and AgO co-modified ZnO nanocomposites for promoting wound healing in Staphylococcus aureus infection, Materials Today Bio 18 (2023) 100552.

[28] G. Pettet, M. Chaplain, D. McElwain, H. Byrne, On the role of angiogenesis in wound healing, Proceedings of the Royal Society of London. Series B: Biological Sciences 263 (1376) (1996) 1487–1493.

[29] A.P. Veith, K. Henderson, A. Spencer, A.D. Sligar, A.B. Baker, Therapeutic strategies for enhancing angiogenesis in wound healing, Adv. Drug Deliv. Rev. 146 (2019) 97–125.

[30] X. He, Y. Qian, C. Wu, J. Feng, X. Sun, Q. Zheng, X. Li, J. Shen, Entropy-mediated high-entropy MXenes nanotherapeutics: NIR-II-enhanced intrinsic oxidase mimic activity to combat methicillin-resistant Staphylococcus Aureus infection, Adv. Mater. 35 (26) (2023) 2211432.

[31] Z. Li, D. Xu, Z. Deng, J. Yin, Y. Qian, J.-T. Hou, X. Ding, J. Shen, X. He, Single-atom-catalyzed MXene-based nanoplatform with photo-enhanced peroxidase-like activity nanotherapeutics for staphylococcus aureus infection, Chem. Eng. J. 452 (2023) 139587.

[32] X. He, Y. Lv, Y. Lin, H. Yu, Y. Zhang, Y. Tong, C. Zhang, Platinum nanoparticles regulated V_2C MXene nanoplatforms with NIR-II enhanced nanozyme effect for photothermal and chemodynamic anti-infective therapy, Adv. Mater. (2024) 2400366.

[33] S. Theivendran, S. Lazarev, C. Yu, Mesoporous silica/organosilica nanoparticles for cancer immunotherapy, Exploration (2023) 20220086.

[34] Y. Jung, Y. Huh, D. Kim, Recent advances in surface engineering of porous silicon nanomaterials for biomedical applications, Microporous Mesoporous Mater. 310 (2021) 110673.

[35] W. Li, Z. Liu, F. Fontana, Y. Ding, D. Liu, J.T. Hirvonen, H.A. Santos, Tailoring porous silicon for biomedical applications: from drug delivery to cancer immunotherapy, Adv. Mater. 30 (24) (2018) 1703740.

[36] W. Duan, J. Zhao, Y. Gao, K. Xu, S. Huang, L. Zeng, J.-W. Shen, Y. Zheng, J. Wu, Porous silicon-based sensing and delivery platforms for wound management applications, J. Contr. Release 371 (2024) 530–554.

[37] W. Duan, Y. Jin, Y. Cui, F. Xi, X. Liu, F. Wo, J. Wu, A co-delivery platform for synergistic promotion of angiogenesis based on biodegradable, therapeutic and self-reporting luminescent porous silicon microparticles, Biomaterials 272 (2021) 120772.

[38] J. Zhao, W. Duan, X. Liu, F. Xi, J. Wu, Microneedle patch integrated with porous silicon confined dual nanozymes for synergistic and hyperthermia-enhanced nanocatalytic ferroptosis treatment of melanoma, Adv. Funct. Mater. 33 (47) (2023) 2308183.

[39] A. Saeed, S. Jain, G.R. Kokil, M.B. Ghasemian, A. Sharma, P. Siwakoti, K. Kalantar-Zadeh, T. Kumeria, On-demand activatable peroxidase-like porous silicon–gold nanozymes for colorimetric sensing, ACS Appl. Nano Mater. 7 (3) (2024) 3289–3299.

[40] W. Duan, J. Zhao, X. Liu, Y. Zheng, J. Wu, Trapping and release of NIR-active dye in porous silicon as a theranostic strategy for ROS photothermal monitoring and chronic wound management, J. Contr. Release 359 (2023) 428–440.

[41] A. Sahu, J. Jeon, M.S. Lee, H.S. Yang, G. Tae, Antioxidant and anti-inflammatory activities of Prussian blue nanozyme promotes full-thickness skin wound healing, Mater. Sci. Eng. C 119 (2021) 111596.

[42] D. Yang, M. Yuan, J. Huang, X. Xiang, H. Pang, Q. Wei, X. Luo, C. Cheng, L. Qiu, L. Ma, Conjugated network supporting highly surface-exposed Ru Site-based artificial antioxidase for efficiently modulating microenvironment and alleviating solar dermatitis, ACS Nano 18 (4) (2024) 3424–3437.

[43] W. Duan, X. Liu, J. Zhao, Y. Zheng, J. Wu, Porous silicon carrier endowed with photothermal and therapeutic effects for synergistic wound disinfection, ACS Appl. Mater. Interfaces 14 (43) (2022) 48368–48383.

[44] Y. Cui, W. Duan, Y. Jin, F. Wo, F. Xi, J. Wu, Graphene quantum dot-decorated luminescent porous silicon dressing for theranostics of diabetic wounds, Acta Biomater. 131 (2021) 544–554.

[45] Y. Jin, Y. Yang, W. Duan, X. Qu, J. Wu, Synergistic and on-demand release of Ag-AMPs loaded on porous silicon nanocarriers for antibacteria and wound healing, ACS Appl. Mater. Interfaces 13 (14) (2021) 16127–16141.

[46] P. Zhai, L. Liu, Y. Wei, J. Zuo, Z. Yang, Q. Chen, F. Zhao, X. Zhang, Y. Gong, Self-healing nucleation seeds induced long-term dendrite-free lithium metal anode, Nano Lett. 21 (18) (2021) 7715–7723.

[47] S.M. Haidary, E.P. Córcoles, N.K. Ali, Folic acid delivery device based on porous silicon nanoparticles synthesized by electrochemical etching, Int. J. Electrochem. Sci. 8 (7) (2013) 9956–9966.

[48] D.-W. Lee, S.-J. Park, S.-K. Ihm, K.-H. Lee, Synthesis of Pt-containing mesoporous silica using Pt precursor as a pore-forming agent, J. Non-Cryst. Solids 353 (16–17) (2007) 1501–1507.

[49] A. Plummer, V. Kuznetsov, J. Gascooke, J. Shapter, N. Voelcker, Combined thermal and FTIR analysis of porous silicon based nano-energetic films, RSC Adv. 7 (12) (2017) 7338–7345.

[50] Y. Huang, D. Li, S. Feng, Y. Jia, S. Guo, X. Wu, M. Chen, W. Shi, Pt atoms/clusters on Ni-phytate-sensitized carbon nitride for enhanced NIR-light-driven overall

water splitting beyond 800 nm, Angew. Chem. Int. Ed. 61 (45) (2022) e202212234.
[51] Y. Zhu, Z. Wang, R. Zhao, Y. Zhou, L. Feng, S. Gai, P. Yang, Pt decorated Ti_3C_2Tx MXene with NIR-II light amplified nanozyme catalytic activity for efficient phototheranostics, ACS Nano 16 (2) (2022) 3105–3118.
[52] X.M. Zhu, H.Y. Wan, H. Jia, L. Liu, J. Wang, Porous Pt nanoparticles with high Near-Infrared photothermal conversion efficiencies for photothermal therapy, Adv. Healthcare Mater. 5 (24) (2016) 3165–3172.
[53] S. Wu, C. Xu, Y. Zhu, L. Zheng, L. Zhang, Y. Hu, B. Yu, Y. Wang, F.J. Xu, Biofilm-sensitive photodynamic nanoparticles for enhanced penetration and antibacterial efficiency, Adv. Funct. Mater. 31 (33) (2021) 2103591.
[54] L.X. Yan, L.J. Chen, X. Zhao, X.P. Yan, pH switchable nanoplatform for in vivo persistent luminescence imaging and precise photothermal therapy of bacterial infection, Adv. Funct. Mater. 30 (14) (2020) 1909042.
[55] D. Chao, Q. Dong, Z. Yu, D. Qi, M. Li, L. Xu, L. Liu, Y. Fang, S. Dong, Specific nanodrug for diabetic chronic wounds based on antioxidase-mimicking MOF-818 nanozymes, J. Am. Chem. Soc. 144 (51) (2022) 23438–23447.
[56] H. Che, J. Xu, D. Wu, S. Chen, C. Liu, C. Zhao, K. Peng, Reactive oxygen species-responsive polydopamine-PtCuTe nanoparticle-loaded microneedle system for promoting the healing of infected skin wounds, J. Contr. Release 376 (2024) 999–1013.
[57] J. Xiang, X. Yang, M. Tan, J. Guo, Y. Ye, J. Deng, Z. Huang, H. Wang, W. Su, J. Cheng, NIR-enhanced Pt single atom/g-C_3N_4 nanozymes as SOD/CAT mimics to rescue ATP energy crisis by regulating oxidative phosphorylation pathway for delaying osteoarthritis progression, Bioact. Mater. 36 (2024) 1–13.
[58] T. Ye, C. Chen, D. Wang, C. Huang, Z. Yan, Y. Chen, X. Jin, X. Wang, X. Ding, C. Shen, Protective effects of Pt-NC single-atom nanozymes against myocardial ischemia-reperfusion injury, Nat. Commun. 15 (1) (2024) 1682.